Technical University of Denmark

DTU

Light-driven micro-robotics for contemporary biophotonics.

Villangca, Mark Jayson; Glückstad, Jesper; Palima, Darwin

Publication date:
2016

Document Version
Publisher's PDF, also known as Version of record

Link back to DTU Orbit

DTU Library
Technical Information Center of Denmark

Light-driven micro-robotics for contemporary biophotonics

Mark Jayson M. Villangca
April 30, 2016

Department of Photonics Engineering
Programmable Phase Optics
Technical University of Denmark
Building 343, 2800 Kgs. Lyngby, Denmark
www.ppo.dk

Preface

This thesis is done as part of the requirement for the PhD study conducted at DTU Fotonik, Technical University of Denmark. The work is primarily done within the Programmable Phase Optics group under the supervision of Professor Jesper Glückstad and co-supervised by Associate Professor Darwin Palima. One of the published works presented in this thesis is done in collaboration with Dr. Duncan Casey from Liverpool John Moores University, Liverpool, UK.

Acknowledgements

PhD has been the most demanding, challenging and yet fulfilling chapter of my life. During this course, I have received help and support from numerous people and to make this thesis possible. First I would like to thank PPO group; Jesper Glückstad, Darwin Palima and Andrew Bañas and the other people who have been with us for some time: Oleksii Kopylov, Camille Scotté, Minqiang Bu and Caro Carrissemoux. I thank the e-space members especially Prof. Toshio Morioka for bringing together a great team. I acknowledge the help from Thomas Aarøe Anhøj and Radu Malureanu with my work in the cleanroom. To our collaborators from University of Copenhagen and University of Vigo, Spain, thank you for bringing in new knowledge to the group. To my fellow PhD students I met at conferences, schools and in the department, listening to your stories especially about how passionate you are to your research has inspired me to do my best. I wish you all good luck.

I thank the thesis committee members for reviewing my work and for their useful comments to improve this thesis.

To the people who keep me in touch with the outside world, I thank my church mates, my friends from the Philippines especially those who decided to pursue their studies away from home, Miguel Sison, Orly Tarun, Irene Crisologo, Mary Grace Bato, Cindyliza Esporlas, Alva Presbitero, Cheryl Abundo, Kaye Vergel and Christian Alis. Thank you for the moral support. To my landlady for checking my initial Danish abstract. And most of all, to my family for their understanding. I dedicate this thesis to you.

Abstract

In the early days of biology, dissection has been the staple for studying the functions of the body and its component organs. The invention of the microscope has paved the way the study of cells, bacteria and other microorganisms. The ability to move such microorganisms or send stimulus in a controlled manner can push our understanding of the dynamics at cellular level. In this regard, the discovery of light's radiation forces becomes important in the field of biology. The field of optical manipulation has evolved from the simple demonstration of radiation forces to more sophisticated trapping setup and trapped objects. This progress has been augmented with improvements in beam shaping techniques, instrumentation and design of trappable objects.

The contribution of this thesis in the optical manipulation literature is to introduce a new set of custom-made trappable objects which we call light-driven micro-robots or light robotics. These are self-contained micro-robots that are designed to perform specific tasks. The first micro-robot that we will present is called the wave-guided optical waveguides (WOWs). The WOWs designed for targeted light delivery where a waveguide structure is fabricated and handles for trapping are attached. The waveguide is coupled with a holography-controlled beam. We have shown three-dimensional movement, tracking and coupling. The second micro-robot is designed for material transport where we have fabricated a vessel that can be trapped and manipulated. In addition, an optically controlled loading and unloading mechanism is built inside the micro-robot. It utilizes photothermal heating to generate convection currents that can draw in and out the cargo. Our results show that we can load and unload cargo which can be an important feature in drug delivery.

This thesis is a documentation on the design and fabrication process, sample preparation, experimental procedure and demonstration of the capabilities of the micro-robots and our outlook on their potential use in biophotonics. As we have used tools as extension of our hands in the early study of biology, we envision these micro-robots to be an extension of optical manipulation for studying further down in the micro-scale.

Resumé

Lige siden de tidlige dage af biologi-udforskningen, har dissektion været kernen i at studere kroppens funktioner og dens organer. Opfindelsen af mikroskopet banede vejen for studiet af celler, bakterier og andre mikroskopiske organismer. Evnen til at flytte mikro-organismer eller sende stimuli ind på en meget kontrolleret og præcis måde kan udvide vores forståelse af dynamikken helt ned på enkelt-celle niveau. I den forbindelse har opdagelsen af lysstrålings-inducerede kræfter været en særdeles vigtig milepæl inden for mikro-biologien. Forskningsområdet optisk mikro-manipulation har udviklet sig dramatisk fra de første simple demonstrationer af lysstrålings-kræfter i enkelt-stråle optiske pincetter til sofistikerede real-time modulationer af multiple samtidige lys-fælder til fastholdelse og manipulation af komplekse mikro- og nano-objekter. Dette fremskridt er blevet stærkt udvidet med de store forbedringer i lys-stråle formning (såkaldt laser beam shaping) og design af specielle 3D-printede mikro- og nano-objekter.

Hovedbidraget i denne afhandling er primært at introducere en hel ny generation af skræddersyede 3D-printede mikro-objekter, som vi har valgt at kalde lys-drevne eller blot optiske mikro-robotter. Hver enkelt af disse optiske mikro-robotter er designet til at kunne udføre helt specifikke opgaver på mikro- og/eller nano-niveau. Den første type mikro-robot som vil blive præsenteret i afhandlingen kaldes for Wave-guided Optical Waveguides (WOWs). Disse WOWs er konstrueret til at kunne guide og målrette lys-afgivelse under diffraktionsgrænsen (i nærfeltet), hvor en avanceret bølgeleder-struktur er integreret sammen med såkaldte "optiske håndtag" til at styre strukturen alene vha. lys. Bølgeleder-strukturen er kombineret på snedig vis med en real-time holografi-kontrolleret vifte af styrbare laser-stråler. Vi har vist fuld tre-dimensionel bevægelse, sporing og ind/ud-kobling af laser-lys med disse WOWs. Den anden type mikro-robot, som introduceres i afhandlingen, er konstrueret til materiale-transport, hvor vi har fremstillet et miniature-fartøj, der kan fungere som en slags mikroskopisk kanyle. Mikro-robotterne har indbygget en ren laser-kontrolleret "suge" og "sprøjte" mekanisme. De udnytter såkaldt foto-termisk opvarmning til at generere en konvektions-strøm, der kan indtrække, transportere og udskubbe en lille last af små partikler. Vores resultater viser, at vi

effektivt kan "laste" og "losse" med denne type mikro-robot med et meget spændende potentiale inden for såkaldt "nano drug delivery" til f.eks. isolerede cirkulerende tumor-celler eller pluri-potente stamceller.

Afhandlingen dokumenterer alle steps fra design, fabrikation, prøveforberedelse, eksperimentelle procedurer og til egentlig demonstration af de fantastiske muligheder, der ligger i brugen af disse nyopfundne optiske mikro-robotter og deres potentielle banebrydende anvendelser inden for nanobiofotonik på enkelt-celle niveau.

Publications

Journal articles

1.   M. Villangca, A. Bañas, D. Palima, and J. Glückstad, "Dynamic diffraction-limited light-coupling of 3D-maneuvered wave-guided optical waveguides," Opt. Express **22**, 17880–17889 (2014).

2.   A. Bañas, D. Palima, M. Villangca, T. Aabo, and J. Glückstad, "GPC light shaper for speckle-free one-and two-photon contiguous pattern excitation," Opt. Express **22**, 5299–5310 (2014).

3.   A. Bañas, O. Kopylov, M. Villangca, D. Palima, and J. Glückstad, "GPC light shaper: static and dynamic experimental demonstrations," Opt. Express **22**, 23759–69 (2014).

4.   M. Villangca, A. Bañas, D. Palima, and J. Glückstad, "GPC-enhanced read-out of holograms," Opt. Commun. **351**, 121–127 (2015).

5.   O. Kopylov, A. Bañas, M. Villangca, and D. Palima, "GPC light shaping a supercontinuum source," Opt. Express **23**, 1894–1905 (2015).

6.   A. Bañas, O. Kopylov, M. Villangca, D. Palima, and J. Glückstad, "GPC : Recent developments," Opt. Data Process. Storage **1**, 22–37 (2015).

7.   M. Villangca, A. Bañas, D. Palima, and J. Glückstad, "Generalized phase contrast-enhanced diffractive coupling to light-driven microtools," Opt. Eng. **54**, 111308 (2015).

8.   M. Villangca, D. Casey, and J. Glückstad, "Optically-controlled platforms for transfection and single- and sub-cellular surgery," Biophys. Rev. **7**, 379–390 (2015).

9.   M. J. Villangca, D. Palima, A. R. Bañas, and J. Glückstad, "Light-driven micro-tool equipped with a syringe function," Light: Science & Applications, Nature Publishing Group (2016). *(Accepted for publication)*

Conference proceedings

1.   M. Villangca, A. Bañas, T. Aabo, D. Palima, and J. Glückstad, "Diffractive beam shaping, tracking and coupling for wave-guided optical waveguides (WOWs)," in *Proc. SPIE 8999, Complex*

Light and Optical Forces VIII, D. L. Andrews, E. J. Galvez, and J. Glückstad, eds. (2014), Vol. 8999, p. 89991F.

2. M. Villangca, A. Bañas, O. Kopylov, D. Palima, and J. Glückstad, "Real-time dynamic coupling of GPC-enhanced diffraction-limited focal spots," in *Proc. SPIE 9379, Complex Light and Optical Forces IX*, E. J. Galvez, J. Glückstad, and D. L. Andrews, eds. (2015), Vol. 9379, pp. 93790M–1–93790M–6.

3. M. Villangca, A. Bañas, O. Kopylov, D. Palima, and J. Glückstad, "Optimal illumination of phase-only diffractive element using GPC light shaper," in *Proc. SPIE 9379, Complex Light and Optical Forces IX*, E. J. Galvez, J. Glückstad, and D. L. Andrews, eds. (2015), Vol. 9379, pp. 93790O–1–93790O–6.

4. J. Glückstad, M. Villangca, A. Bañas, and D. Palima, "Holographic 3D tracking of microscopic tools," in *Proc. SPIE 9477, Optical Pattern Recognition XXVI*, D. Casasent and M. S. Alam, eds. (2015), p. 947702. *(Invited contribution)*

5. D. Palima, M. J. Villangca, A. R. Bañas, O. Kopylov, and J. Glückstad, "Spatial modulation conjugate to the target plane: beamshaping, micromanipulation and microscopy," in *Northern Optics and Photonics*, Lappeenranta, Finland (2015). *(Invited contribution)*

6. M. Villangca, D. Palima, A. Bañas, and J. Glückstad, "Photothermal heating in metal-embedded microtools for material transport," in *Proc. of SPIE*, J. Glückstad, D. L. Andrews, and E. J. Galvez, eds. (2016), Vol. 9764, p. 97641F. *(Invited contribution)*

7. J. Glückstad, D. Palima, M. Villangca, and A. Banas, "3D light robotics," in *Proc. SPIE 9738, Laser 3D Manufacturing III*, B. Gu, H. Helvajian, and A. Piqué, eds. (2016), p. 97380A. *(Invited contribution)*

8. A. R. Bañas, M. J. Villangca, D. Palima, and J. Glückstad, "Dark GPC," in *Proc. SPIE 9764, Complex Light and Optical Forces X*, J. Glückstad, D. L. Andrews, and E. J. Galvez, eds. (2016), p. 97640H.

9. D. Palima, A. R. Bañas, M. J. Villangca, and J. Glückstad, "GPC and quantitative phase imaging," in *Proc. SPIE 9718, Quantitative Phase Imaging II*, G. Popescu and Y. Park, eds. (2016), p. 97182P. *(Invited contribution)*

10. A. Bañas, D. Palima, M. Villangca, and J. Glückstad, "Cell sorting using efficient light shaping approaches," in *Proc. SPIE 9764,*

Complex Light and Optical Forces X, J. Glückstad, D. L. Andrews, and E. J. Galvez, eds. (2016), p. 97640F.

Presentations at conferences, workshops and seminars

1. J. Glückstad, D. Palima, A. R. Bañas, and M. J. Villangca, "New two-photon sculpting of light and matter for nanobiophotonics and parallel optogenetics," in *Proceedings of EOS Topical Meetings at Capri 2013* (European Optical Society, 2013). *(Invited contribution)*

2. A. R. Bañas, D. Palima, M. J. Villangca, T. Aabo, and J. Glückstad, "Unmanned" optical micromanipulation using waveguide microstructures," in *Proceedings of the EU COST Workshop* (2013).

3. D. Palima, A. R. Bañas, M. J. Villangca, T. Aabo, and J. Glückstad, "Generalized Phase contrast and matched filtering for speckle-free patterned illumination," in *Spatially Precise Optogenetics at Depth Incubator Meeting* (Optical Society of America (OSA), 2013).

4. J. Glückstad, A. R. Bañas, D. Palima, T. Aabo, and M. J. Villangca, "Sculpted light and matter for nanobiophotonics and two-photon optogenetics," in *NanoBioTech -Montreux,* Montreux, Switzerland (2013).

5. M. J. Villangca, A. R. Bañas, T. Aabo, D. Palima, and J. Glückstad, "Comparing temporally-focused GPC and CGH for two-photon excitation and optogenetics in turbid media," in *546. WE Hereaus Seminar: Light in Disordered Photonics Media,* Germany (2013).

6. A. R. Bañas, O. Kopylov, M. J. Villangca, D. Palima, and J. Glückstad, "Efficient shaping of light," in *Photonics Seminar,* Singapore (2014).

7. M. J. Villangca, A. R. Bañas, D. Palima, and J. Glückstad, "Structure-mediated nano-biophotonics," in *Photonics Seminar,* Singapore (2014).

8. J. Glückstad, M. J. Villangca, A. R. Bañas, and D. Palima, "Wave-guided Optical Waveguides tracked and coupled using dynamic diffractive optics," in *Workshop on Information Optics WIO2014 ,* Neuchâtel, Switzerland (2014).

9. A. R. Bañas, D. Palima, M. J. Villangca, T. Aabo, and J. Glückstad, "GPC Light Shaper for energy efficient laser materials

processing," in *15th International Symposium on Laser Precision Microfabrication,* Vilnius, Lithuania (2014).

10. J. Glückstad, M. J. Villangca, A. R. Bañas, and D. Palima, "Light-printed, light-driven and light-coupling micro-tools for contemporary nano-biophotonics," in *NanoBioTech-Montreux,* Montreux, Switzerland (2014).

11. J. Glückstad, A. R. Bañas, M. J. Villangca, and D. Palima, "Wavefront Control by GPC," in *Adaptive Optics and Wavefront Control in Microscopy and Ophthalmology,* Paris, France (2015).

12. M. J. Villangca, A. R. Bañas, D. Palima, and J. Glückstad, "Wave-guided Optical Waveguides: Towards sculpted sub-micron light-matter interaction for broadband sources," in *2nd Opt. Nanospectroscopy Conf.* Dublin, Ireland (2015).

13. A. R. Bañas, O. Kopylov, P. Raaby, D. Palima, M. J. Villangca, and J. Glückstad, "Efficient illumination of spatial light modulators for optical trapping and manipulation," in *Trends Opt. Micromanipulation III*, Obergurgl, Austria (2015).

14. D. Palima, M. J. Villangca, A. R. Bañas, O. Kopylov, and J. Glückstad, "Quantitative phase in microscopy: back-to-basics measurements," in *Focus on Microscopy, Göttingen, Germany.* (2015).

15. J. Glückstad, D. Palima, A. R. Bañas, and M. J. Villangca, "Novel light-driven micro-robotics," in *Proceedings of 6th EOS Topical Meeting on Optical Microsystems* (2015). *(Postdeadline)*

16. J. Glückstad, D. Palima, M. J. Villangca, and A. R. Bañas, "Sculpting light for new biophotonics applications," in *The 23th Annual International Conference on Advanced Laser Technologies*, Farø, Portugal (2015).

17. J. Glückstad, D. Palima, M. J. Villangca, and A. R. Bañas, "Advanced light sculpting for contemporary biophotonics," in *Neurophotonics Seminar,* Baltimore, United States (2015).

18. J. Glückstad, D. Palima, M. J. Villangca, and A. R. Bañas, "Active Light Shaping using GPC," in *10th International Workshop on Adaptive Optics for Industry and Medicine,* Padova, Italy (2015).

19. J. Glückstad, M. J. Villangca, A. R. Bañas, and D. Palima, "Structure-mediated nano-biophotonics," in *36th Progress In Electromagnetics Research Symposium, 2015,* Prague (Electromagnetics Academy, 2015).

20.   A. R. Bañas, D. Palima, M. J. Villangca, O. Kopylov, and J. Glückstad, "Supercontinuum light shaping with GPC," in *Cost Action MP1205 ,* Porto, Portugal (2015).

Contents

Table of Contents

1. Introduction

The use of radiation forces to manipulate minute particles has opened a new area where light can be used as our "gentle hands" to get hold of the microscopic world. With such ability, we have pushed our understanding of biology. By being able to send stimulus in a controlled manner, we can understand the dynamics of biological microsystems. Aside from manipulating live cells to understand their growth as in the budding of yeast or how they respond in close proximity with other cells, we have learned to functionalize microbeads and attach them to cells or DNA strand for force or membrane elasticity measurements.

Given the importance of understanding biology in the microscale, we have developed micro-robots to extend optical trapping with new functionalities. In this chapter we will first start with a broad discussion of micro-robotics and the advantages of "miniaturizing" our macroscopic tools and the challenges in moving to such small scale. The rest of the thesis will cover our own light-based micro-robots, their fabrication and actuation as well as our outlook in their applications to contemporary biophotonics.

1.1. Micro-robotics

Robotics has found its uses in industry where some of the repetitive, tedious, precise and dangerous tasks are now performed by machines. What a wonderful thing it could be if we can scale that down in the microscale! In the inspiring and prophetic talk of Richard Feynman back in 1959 entitled, "There's Plenty of Room at the Bottom" [1], he mentioned the possibilities of bringing down the scale of everyday objects such as an entire library. Doing so would reduce the storage that is needed and thus allowing "plenty of room" for other things such as all the books in the world. He also went further by imagining if we could swallow a surgeon and do surgery from within. Incidentally, a film called "Fantastic Voyage" was made in 1966 that is exactly about that. The ability to make tiny machines allows us to reach places and perform tasks that we cannot do or otherwise are invasive simply because we are too big. Another advantage of miniaturization is economical fabrication since only a small amount of material is needed and the whole process can be parallelized. The strength of micro-robotics lies with the

possibility of controlling multiple machines independently [2]. The above examples sound like they are from science fiction however with current fabrication techniques mostly from semiconductor industry these can become possible. We just have to rethink our view of the microscopic world since our intuition of the macroscopic world may not always apply.

It is a great challenge to build, power and control tiny machines to perform specific tasks. Micro-robotics is not simply about making things smaller. Although the laws of physics are the same, the small dimensions involved in micro-robotics can drastically affect which phenomena dominate [3–6]. These effects can be separated as volume or bulk and surface related. Volume related properties and effects include mass, weight, heat capacity and body forces. Surface related properties and effects include friction, heat transfer and surface forces. Consider a characteristic length, L, volume scales as $\sim L^3$ while surface scales as $\sim L^2$. As the characteristic length becomes smaller, we can see that surface effects become more significant. For example, the weight of a micro-robot will not matter but adhesion forces such as van der Waals force is a major consideration (i.e. surfaces becomes sticky). Thus we need to rethink how to implement macroscopic mechanisms such as pumping, rotation of rotors, sliding and the like. Fluid dynamics also differs with our everyday experiences that are characterized by a high Reynolds number where we can see turbulence in fluid flow around an object. The Reynolds number quantifies the interaction of the fluid's inertia and viscosity as it flows around an object and it is given by

$$Re = \frac{\rho V_s L}{\eta} \qquad (1.1)$$

where ρ, η and V_s are the fluid density, viscosity and free-stream velocity are characteristic of the system respectively. As the characteristic length L of an object goes down, the Re goes down and we arrived at more laminar fluid flow even around the object and viscous forces dominate. The viscous drag thus eliminates momentum-based movement of microscopic objects [7].

Aside from dealing with physical effects due to small dimensions, another challenge is how to actuate or power up the micro-robots. A

micro-robot should ideally be self-contained. This means that the parts, the actuation mechanism are built-in or can be supplied externally for it to perform its designed function. However, conventional power supplies such as batteries are also affected by scaling of physical effects. The amount of energy that is required and that also can be stored scales down. However, it is not straightforward or to similarly scale down the structure of batteries or other form of power supplies. Power supplies that rely on surface area are more suitable such as solar cells or even chemical reactions from the environment. Actuation can also come from external sources such electric and magnetic fields and optical forces.

One of the earliest demonstrations of tiny machines powered externally by chemical fuel is the catalytic nanorods. These are composed of platinum and gold at defined zones that catalyze the decomposition of hydrogen peroxide (H_2O_2) to propel them. Nickel is added to the nanorods so that they can be guided externally by magnets. The linear speed can reach up to 20 μm s^{-1} depending on the concentration of the H_2O_2 [7,8]. An improvement on this design uses rolled-up thin film of InGaAs/GaAs/Cr/Pt and can reach speeds of up to 110 μm s^{-1}. The rolled-up nanotools can be designed to perform corkscrew motions and have been demonstrated to be capable of penetrating a fixed HeLa cell [9]. 3D-printed "microfish" using the same propulsion mechanism have been demonstrated and applied in detoxification [10].

Flagella and cilia are nature's best structure for locomotion at low Re [4,5]. The whip-like rotary motion of these structures allows movement for microorganisms. Recently, an approach to attach living bacterial flagella motors in a synthetic structure has been presented [11]. The purpose was to construct a bio-hybrid micro-robot that can move autonomously, or be guided by chemical gradients, while the synthetic structure can be designed to accommodate drug delivery.

In these examples, chemical fuel from the medium is utilized to power the tiny machines. Chemical fuel can provide high propulsion power. In the case of catalytic nanorods, however, the challenge is the compatibility issues of the fuel with biological samples [12].

Nanowires have also been used for sub-cellular drug delivery with precise control using electric fields [13]. Orthogonal electrodes attached to a special container made of PMMA where opposite pairs is either operating on AC or DC currents. The movement speed of the nanowires is comparable to catalytic nanorods.

The above mechanism of actuation elegantly addressed the constraints of having small dimensions and on top of that being able to perform tasks such as cell membrane disruption and cargo delivery. However, there are limitations with these mechanisms. Magnetic control requires the inclusion of nickel which is inherently toxic to living systems. Also, magnetic, electric and chemical gradient controls are difficult to realize for 3D-manipulation [14,15]. Parallelizing the control of multiple micro-robots will also be difficult.

In the next section, we will discuss micro-robots which use light as the actuation mechanism. Although optical forces are not as strong as external fields and chemical-based actuations, optimizations can be made on the shaping of light and the micro-robots. Furthermore, light-based actuation such as optical trapping is fairly straightforward to parallelize and extend to multiple objects.

1.2. Light-driven micro-robotics

Light is an attractive mechanism for powering tiny machines. Advanced control over natural or fabricated micro- or nano-structures using light has been demonstrated throughout the years starting with the pioneering work of Ashkin [16]. Developments in pulsed lasers, light-curing polymers and complex optical trapping mechanisms all serve to catalyze the advent of more complex light-based micro machines and thus the emergence of so-called light robotics [17]. The fabrication of a microscopic bull with nano-features by Kawata *et al* [18] is a popular example of the precision and control that one can achieve with 3D-printing based on two-photon absorption of light sensitive polymers with the earliest work dating back to the mid 90's [19]. From there on, gradually more sophisticated micro- and nano-structures mimicking macroscopic tools have been first light-fabricated and subsequently light-actuated. A functional micro-oscillatory system has been made and proposed as a mean to investigate the mechanical properties of minute

objects [18]. There have been reports on microscopic gears [20,21], pumps [22] and even sophisticated light foils [23,24] that have all been first fabricated and subsequently driven by light only.

The hallmark of light robotics is the use of light for fabrication, active actuation and control. One approach, akin to traditional robotics, exploits materials that can exhibit light-activated contraction to work as artificial muscles. A typical example is the recently reported microscopic walkers, which uses contraction of liquid crystal elastomers for locomotion [25]. Another interesting modality is made possible through the use of parallel optical trapping whether holographic [26–28] or Generalized Phase Contrast (GPC) based [29–31]. Progress in optical manipulation has been boosted by novel technologies such as provided by graphics processing units and advanced spatial light modulators that can enable calculation and generation of real-time multi-beam trapping configurations [32]. Advanced optical traps can be controlled independently or orchestrated to move a plurality of microscopic objects simultaneously in a volume or confined to a plane. This has been successfully demonstrated in applications such as for optical assembly [33–35] and particle sorting [36–38]. An early demonstration of the feasibility of light robotics is in real-time 3D manipulation of custom-fabricated micro-robots made from silica [39]. The micro-robots were optically translated, rotated and tilted thus demonstrating all six-degrees-of-freedom which is a crucial requirement for light robotics to perform delicate tasks such as surface imaging and force measurements [40,41]. This has been further improved with two-photon fabricated tools to the level where the achieved lateral resolution is ca. 200 nm and with an impressive depth resolution of 10 nm [42,43]. Other functionalities such as surface-enhanced Raman spectroscopy [44] and fluorescence enhancement [45] have been demonstrated using metal-coated micro-robots. The flexibility in microfabrication even allows the possibility to optimize the shape of micro-robots to maximize momentum transfer [23,46–48] or force clamping [43,49]. Similar optimizations can be made on the trapping light by using position clamping [50], efficient illumination [51,52] or using adaptive structured illumination [53]. Although light may not be as powerful as the micro-grippers or chemical fuel, light can trigger

secondary effects which, when channeled properly can be effective in accomplishing different tasks.

This thesis will cover our body of work on light robotics. These include targeted-light delivery using two-photon fabricated waveguide structures and a micro-vessel for material transport with an optically controlled pumping mechanism. We will also present optimization in the illuminating laser beam for our devices used in the experiments. We will end this thesis with a summary of our work and our outlook on the potential applications of our micro-robots in contemporary biophotonics.

2. Light and Matter Shaping

Light-driven micro-robotics is primarily based on two important concepts: optical manipulation and microfabrication. This chapter will deal with the aforementioned concepts starting with the scalar treatment of light field, which forms the basis of light shaping that is relevant to optical manipulation and, to some extent, also with microfabrication. Two of the most prominent light shaping modalities are holography and the Generalized Phase Contrast (GPC) method. We start with a discussion of Fourier optics as this will be the basis of the beam shaping techniques mentioned. This is followed by a brief overview of optical trapping using the above light shaping modalities. Matter shaping is in the form of two-photon fabrication. Here we discuss two-photon fabrication as a versatile method to fabricate customized 3D microstructure that can be optically manipulated. We cite examples from literature of the various functionalities and applications that are possible with light-driven micro-robotics.

2.1. Fourier optics

When dealing with linear, isotropic and homogenous medium each component of the electric and magnetic field in the source-free Maxwell's equations follow the same wave equation given by

$$\nabla^2\psi - \frac{n^2}{c^2}\frac{\partial^2\psi}{\partial^2 t} = 0 \tag{2.0}$$

The above assumption holds for the purpose in this thesis since we will be dealing with free-space propagation or homogenous trapping medium and low numerical aperture objective lenses (i.e. NA = 0.55). Thus, with these assumptions, we can treat light, an electromagnetic radiation, as a scalar quantity. Doing so can simplify propagation equations and this will form the basis of the beam shaping techniques that will be discussed in the succeeding sections.

General solutions to equation (2.0) are plane waves and spherical waves. However we will be dealing with superposition of plane waves throughout this thesis and so we put emphasis on this case. Given a time harmonic field distribution $\psi = u(x,y,z)\exp(-i2\pi\nu t)$ and substituting into the wave equation yields the time-independent Helmholtz equation given by

$$\left(\nabla^2 + k^2\right)u = 0 \tag{2.0}$$

where $u(x,y,z)$ is the complex amplitude, $k = \frac{2\pi}{\lambda}$ and $\lambda = \frac{c}{n\nu}$. A detailed derivation on the solution of the Helmholtz equation can be found in standard references such as ref. [54] and we will only quote the final solution given by

$$u(x,y,z) = \iint_{-\infty}^{\infty} U\left(f_x, f_y\right)\Big|_{z=0} \exp\left[i\frac{2\pi z}{\lambda}\sqrt{1 - \left(\lambda f_x\right)^2 - \left(\lambda f_y\right)^2}\right]$$
$$\times \exp\left[i2\pi\left(f_x x + f_y y\right)\right]\mathrm{d}f_x\mathrm{d}f_y \tag{2.1}$$

where $U\left(f_x, f_y\right)\Big|_{z=0}$ is the angular spectrum of the initial field $u(x,y,z=0)$, λ is the wavelength, and (f_x, f_y) are the spatial frequencies. Equation (2.1) implies that $u(x,y,z)$ is a weighted sum of plane waves and thus an inverse Fourier transform. This is a powerful result as it significantly simplifies numerical calculation compared to the full Maxwell's equation treatment. The linearity and shift property of the Fourier transform will also prove useful in hologram calculations for optical trapping. Other approximations (e.g. Fresnel and Fraunhofer) can be made to arrive at different propagation integrals. Using these integrals we can model common optical components such as a lens. It turns out that a lens performs a Fourier transform of the input at the back focal plane. This result is relevant in holographic addressing that will be discussed in the later chapters.

2.2. Beam shaping techniques

Now that we know how light propagates and how a lens affects field distributions, we can now design an input field that will result in a desired output field after going through our optical system. The topic of beam shaping is a broad area and has important applications in optical manipulation especially in a biological context and materials processing.

The transverse complex amplitude $u(x,y)$ can be written as $A(x,y)\exp\left[i\varphi(x,y)\right]$ where A is the real-valued amplitude and φ is the phase. Thus beam shaping can be an amplitude modulation, a phase modulation or modulation of both. Amplitude modulation is done by masking or absorption which subtractively changes A. This approach is

quite fast and simple as the mask can be the desired intensity distribution. This is applied in photolithography where UV light is blocked by a mask corresponding to the pattern to be imprinted. Digital micro-mirror devices allow dynamic projection of amplitude patterns. One drawback of this method is that it is inefficient as photons are inevitably wasted to define a bright foreground pattern. Phase modulation involves changing the phase term by passing the field through transparent elements such as phase masks or bleached photographic films. Phase modulation can be more efficient than amplitude modulation since phase masks have low absorption. However, phase modulation may involve optimization algorithms to achieve the desired intensity distribution. Devices such as phase-only spatial light modulators have enabled projection of dynamic patterns by changing the phase of an incident light field. This section will focus on different phase modulation techniques that are relevant in this thesis.

2.2.1. Digital holography

Holography was proposed by Gabor in 1948 as a "new" principle that allows recording of both amplitude and phase in an interference pattern called holograms [55]. Gabor observed that these holograms are records of three-dimensional or planar objects. The setup proposed by Gabor, as shown in Figure 2.1, uses a common path interferometer where a small object is placed after a focus point. The disturbance caused by the small object (i.e. object beam) and the unperturbed portion of the incident beam (i.e. reference beam) interferes at the photographic plate. The recorded interference pattern or hologram can then be used to reconstruct the field distribution by illuminating it with the reference beam. The result is a field distribution that makes it appear that the object is present. One problem with the common path setup is that the reference and conjugate twin image of the reconstructed field is along the same optical path and thus causes crosstalk. An improved version of the original Gabor setup is the off-axis holography setup proposed by Leith and Upatnieks in 1962 [56] which solves the twin image problem.
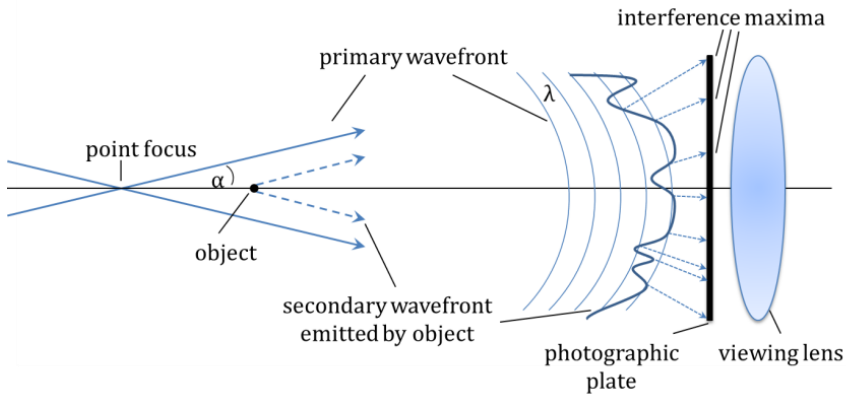
Figure 2.1. Holography setup proposed by Gabor. Image is adapted from [55].

Photographic film-based holography is used for storing volume information of a static object and thus hinders its applicability for moving objects. Today, this photographic film is replaced by liquid crystal-on-silicon (LCoS) devices that can be modified dynamically (see Figure 2.2). In these devices the wavefront curvature are digitally encoded from pre-calculated field distributions using the equations discussed earlier. Dynamic projection of holograms allows the creation of holographic optical tweezers which has important applications in biology. Optical trapping will be discussed later in this chapter.
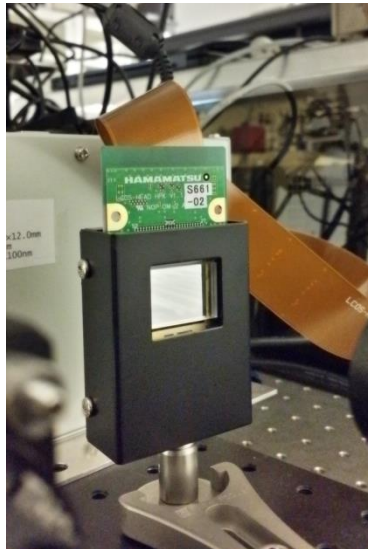
Figure 2.2. A liquid crystal-on-silicon device for dynamic hologram projection.

Aside from optical tweezers, other special beams like Bessel beams and Laguerre-Gaussian beams can be simply projected with an SLM instead of using static phase plates. Iterative optimization algorithms can also be employed to design arbitrary light patterns. In this thesis, we will be using an adaptive Gerchberg-Saxton algorithm which will be discussed in Chapter 4. In practice, digital holography is performed in a $2f$ or optical Fourier transform geometry where focusing gives holographically generated spots strong axial confinements making them suitable for optical manipulation (e.g. holographic optical tweezers) [26,57,58] and other exotic beams [59,60]. Structured light using holography has been shown to improve trapping performance by orders of magnitude [61].

2.2.2. Generalized phase contrast method

Another beam shaping technique is the Generalized Phase Contrast (GPC) which is a generalization of the Zernike phase contrast method. It uses a common path interferometer to do a direct phase-to-intensity mapping. Unlike digital holography, GPC uses a $4f$ imaging setup and makes a point-to-point mapping of phase to intensity. Thus, projection of arbitrary light patterns has no computational overhead. In addition, extended light patterns do not suffer from speckles. However, the one-to-one mapping of GPC limits the attainable maximum output intensities as compared to holography that can integrate light into foci. This makes axial confinement weaker but can be overcome by using counter-propagating beams in optical manipulation. As illustrated in Figure 2.3, GPC works by taking the Fourier transform of an input field using the first lens. At the plane of the phase contrast filter (PCF), the low spatial frequencies are π-phase shifted to generate the so-called synthetic reference wave (SRW) which will interfere to the imaged input field upon passing through the second lens. The interference of the SRW and imaged input field forms the intensity image of the input phase.
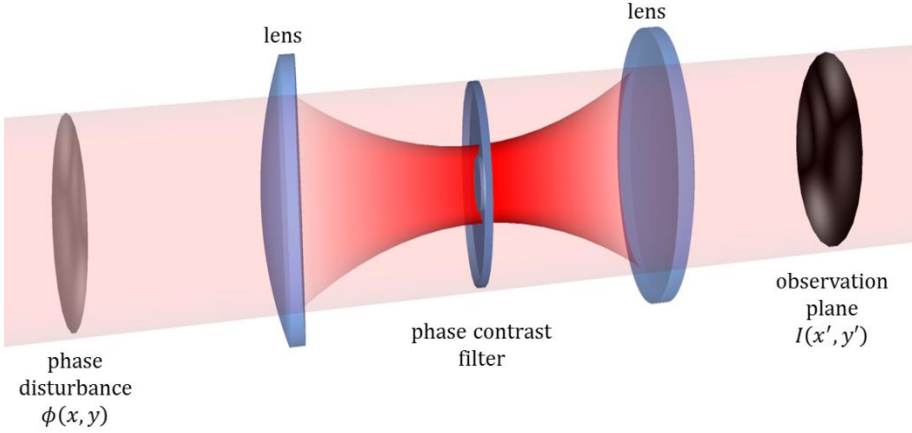
Figure 2.3. Schematic of the Generalized Phase Contrast method. An input phase is converted into an intensity pattern through interference of the synthetic reference and the scattered light.

Optimization of GPC using appropriate phase masks and phase contrast filters will be discussed briefly. In this thesis, we will deal with the use of GPC for efficient illumination of diffractive elements and for enhanced light delivery of optically actuated micro-robots.

2.3. Optical trapping

A fundamental challenge in biology is to be able to directly manipulate cells and their environs while maintaining their sterility and viability. Optical trapping presents an ideal solution: a contact-free force that can be applied through the walls of a cell culture chamber via an infrared wavelength of light that is negligibly absorbed by biological tissue. When focused to a diffraction-limited spot at high numerical apertures, objects can be trapped in three dimensions (i.e. optical tweezers), which can then be controlled and moved relative to their environment using either the optics of the laser system or the stage and focus of a microscope.

Ashkin's pioneering work on lasers provided the first clues to the phenomenon, when he observed that micron-sized particles can be accelerated by radiation pressure alone [62]. This effect arises from the change of momentum of a photon as it is scattered by an object: this in

turn creates an equal and opposite force pushing back towards the most intense region of the laser beam. One component of this force is called the gradient force which, as the name implies, depends in the gradient of the intensity of the trapping beam. Another component, called the scattering force, pushes the particle along the direction of the beam propagation and depends on the intensity of the beam (see Figure 2.4). This photon pressure is the same effect used by solar sails, such as the recent successful demonstration of the IKAROS probe [63]: however, in optical trapping the beam shape is controlled to provide a single energy well that is able to overcome the Brownian motion of the particle, and with which an object can be manipulated.
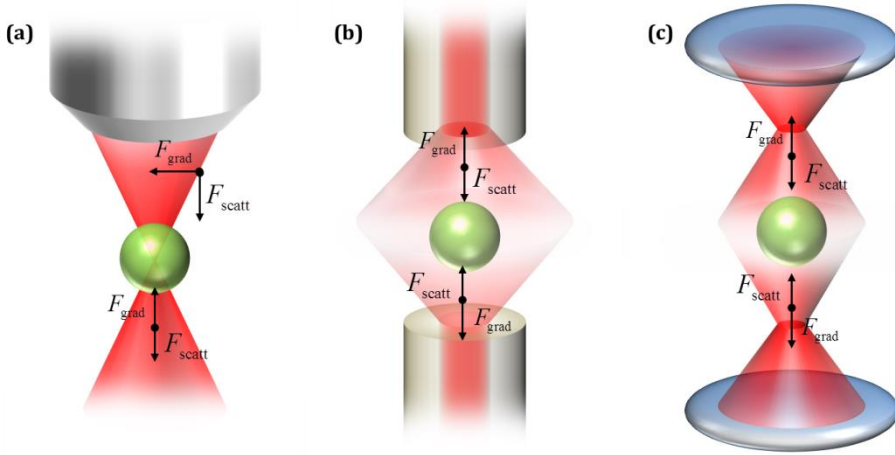
Figure 2.4. Different optical trapping geometries. (a) a tightly focused single beam trap uses gradient forces to keep the particle within the high intensity region. Counter-propagating beam traps such as using (b) opposing fibers and (c) generalized phase contrast (GPC) uses the balance of scattering forces. The arrows indicate the direction of forces. Image is adapted from [64].

Optical trapping is categorized depending on the size of the trapped particle relative to the wavelength of the trapping beam. In the geometric regime where the radius a of the particle is much larger than the wavelength ($a \gg \lambda$), ray optics are sufficient to describe the strength and direction of the optical forces. In the Rayleigh regime (

$a \ll \lambda$) the trapped particle can be treated as a dipole. Mathematically, the forces in this regime are given by

$$F_{grad} = \frac{2\pi a}{c\varepsilon_0 n_m} \nabla I_0 \qquad (2.1)$$

$$F_{scatt} = \frac{I_0 \sigma n_m}{c} \qquad (2.1)$$

where I_0 is the intensity of the trapping beam, c is the speed of light in vacuum, n_m is the index of refraction of the medium, α is polarizability of the particle and σ is the scattering cross section. Both the polarizability and scattering cross section depends on the ratio of the index of refraction of the particle n_p and the medium. Between them lies the Mie regime where the particle size is comparable to the wavelength ($0.1-10\lambda$). Most biological samples lie in this range. In this regime, electromagnetic field theory [65,66] can be used to calculate the forces. Force calculation in optical traps is discussed in the work of Rohrbach and Stelzer [67] and a computational toolbox is presented by Nieminen et al [68].

A common approach to create single beam gradient force trap is to use high numerical aperture (NA) objective lenses. These lenses generate a tight cone of light forming a beam waist: for a beam with a Gaussian profile, the maximum intensity (and thus maximum trapping force) is to be found at this waist. The versatility of optical tweezers has progressed with the advent of spatial light modulators (SLM) [69]. These systems are generally (although not exclusively) rapid switching liquid crystal (LCD) screens, which may be programmed to display patterns to diffract incoming laser beams into tight foci. Multiple patterns can be generated on the same SLM and the diffracting patterns rapidly recalculated, generating large numbers of individually addressable traps which can be dynamically altered in three dimensions [70,71].

High NA lenses impose their limitations, however. A tight cone angle imposes a short working distance (< 250 μm) and typically requires an oil or water immersion lens. This is impractical for many on-chip applications, while experiments requiring elevated temperatures become problematic as heat is conducted through the objective body,

resulting in both optical aberrations and extended equilibration times. As a result, SLM beam shaping has been used to generate a number of other beam profiles. For example, Bessel beams comprising concentric rings of light are (for the purposes of microscopy and trapping) non-diffracting, leading to their application in longer-range trapping and sorting experiments. The discussion of Bessel beams and related light-sculpting is beyond the scope of this thesis, but the interested reader is directed to comprehensive reviews by McGloin and Dholakia [72] and Woerdemann [60]. The applicability of such exotic beam to trapping and micromanipulation applications was recently demonstrated by Ruffner and Grier [73] by coherently superposing coaxial Bessel beams to create a so-called "tractor beams" .

A number of other modalities for extending or altering trapping geometries also exist: for example, a trapping effect similar to that of a high-NA lens can be generated using a tapered optical fiber, which provides both a simple technique for the introduction of a beam orthogonal to the viewing plane but also permits the simple organization of microparticles into ordered patterns and geometries [74]. Another possible trapping configuration, the dual-beam trap, uses counter-propagating beams. This has been demonstrated using optical fibers [75] and extended to multiple dynamic traps using Generalized Phase Contrast (GPC) -based trapping beams [76]. Counter-propagating beams can also be used with lower NA objective lenses. The long working distance offered by these types of microscope objectives allows a side imaging configuration providing a more intuitive optical trapping in 3D [77]. Counter-propagating beams use the scattering force for axial trapping, and the axial movement of the trap is controlled by varying the ratio of the intensities of the beams. Because single-beam 3D optical traps become less stable as particle size increases, counter-propagating beams are more suited to larger objects. The less stringent requirement for a tight focus in counter-propagating beams also prevents photodamage for live samples [78].

The different optical trapping methods mentioned above can provide a way to "hold" and move the micro-robots. In our experiments, we will be using multiple counter-propagating beams for manipulating the micro-robots and take advantage of the large working distance for side-

imaging. The next section will discuss two-photon absorption that is used to fabricate complex 3D micro-robots

2.4. Two-photon fabrication

Trapping of microbeads has been a staple of optical manipulation. Many discoveries especially in biology has used functionalized micro-beads for elasticity measurement [79], porous beads for drug delivery [80], and many more examples in literature [81]. Trap stiffness is extensively studied with some authors providing computational toolbox to calculate this [68].

Since the shape of the trapped structure highly influences the optical trapping force, microfabrication is an equally interesting topic. Microfabrication and nanofabrication are terminologies associated with semiconductors. Here, the above techniques are confined to 2D structures and moving to 3D requires successive deposition of material. This limits the design that can be made. For a true 3D lithography, we will use a nonlinear two-photon absorption process. Two-photon absorption (TPA) processes enable the 3D localized polymerization of photoresists. Photoresists are normally designed to be sensitive in the UV range. Upon absorption of a UV photon, chemical reactions take place which ultimately leads to formation of a solid polymer. In two-photon absorption process, less energetic photon (normally in NIR range) is absorbed by a molecule creating a virtual state which last for a few femtoseconds [82]. While this virtual state is present, the molecule absorbs another photon which completes the jump to excited state (i.e. quadratic dependence on intensity). A comparison of single photon absorption is shown in Figure 2.5. TPA is a rare event and happens at high photon flux. This allows photopolymerization to happen only at the vicinity of the focus. This localization allows the fabrication of fine details and combining this nonlinear process with 3D scanning makes lithography of complex extended objects possible. The first demonstration of three-dimensional microfabrication was made in the 90's by fabricating a spiral structure [19], which later on was used as a microscopic oscillator [18]. The recent commercial availability of two-photon fabrication systems has made rapid prototyping of microstructures possible.
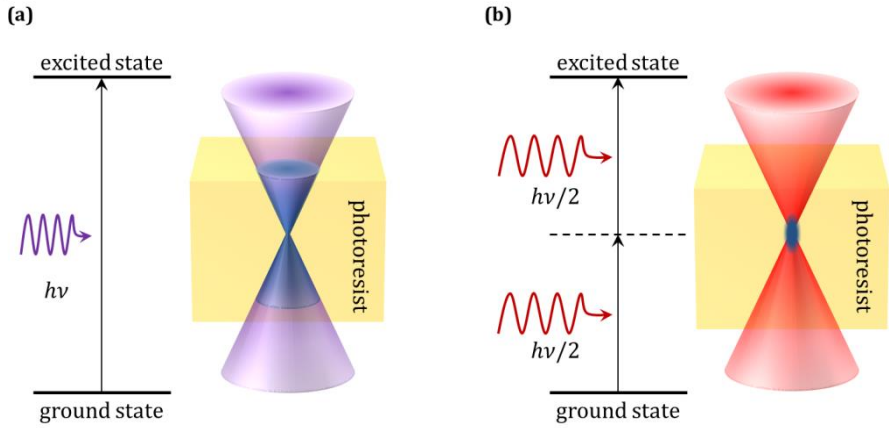
Figure 2.5. A comparison of (a) single-photon and (b) two-photon absorption process. In single-photon absorption, a high energy photon is absorbed by the UV sensitive photoresist within the illuminated volume. Two-photon absorption uses two low energy photons that are absorbed simultaneously to transcend from ground to excited state. This event is rare and only happens at the focus where the photon flux is high.

The chemical properties of the phototoresist also determine the smallest feature size that can be achieved with two-photon fabrication. Photoresists consist of monomers, oligomers, photoinitiators and photosensitizers. Photoinitators create free radicals that start photopolymerization of monomers and oligomers. Sometimes it is necessary to add photosensitizers to improve light absorption and production of radicals. The combination of these components can impact the quality of the fabricated structure. In the fabricated structures presented in this thesis, we use a commercial photoresist. However, one can create his/her own recipe. For a more detailed discussion on the chemistry involved in TPA, the reader is referred to references [82,83].

2.5. Summary

In this chapter, we have discussed the various light and matter shaping techniques in this thesis. The most interesting aspect is the interplay between the two and the possibility of optimizing both [17,24]. In this thesis we will cover a light-sculpted micro-robot for light guiding and

delivery [84–86] as will be discussed in Chapter 3. Some examples that will be cited takes advantage of material shaping for tailored momentum transfer [23,43,47]. The GPC method will be used as a light shaping technique for optimal coupling through these light-guiding micro-robots and will be discussed in Chapter 4. A new generation of micro-robots which uses light-induced secondary effects for material transport is covered in Chapter 5

3. Holographic coupling of wave-guided optical waveguide

One example of light-fabricated and light-driven micro-robot is the wave-guided optical waveguides (WOWs) [84]. These are two-photon fabricated microstructures which consist of a waveguide with spherical handles designated for optical manipulation. Earlier reports on the capability of the WOWs show light guiding and confinement, and targeted light delivery. As the WOWs are maneuvered in 3D space, it is important to maintain efficient coupling through the waveguide structure for the aforementioned functionalities. In order to accomplish that, we have made improvements in our optical trapping setup by adding a holography setup. The inclusion of a holography setup allows dynamic beam shaping of the coupling light and thus helps maintain the functionality of the WOWs.

In this chapter, we discuss how the design and fabrication process of the WOWs as well as the collection from the substrate for optical manipulation and coupling experiments. The details of the optical trapping setup will be presented here will also be relevant for the succeeding chapters. Finally, we combine optical manipulation and holographic coupling for a full 3D targeted light delivery will be presented.

3.1. Fabrication and collection of micro-robots

The WOWs are composed of a free-standing bent waveguide with a tapering end that is attached to sphere handles for optical manipulation with six degrees of freedom, as shown in Figure 3.1. This design is chosen to perform targeted light-delivery in odd geometries that is not possible with traditional trapping approaches. The fabrication has been done using a commercial two-photon photopolymerization setup (Nanoscribe Photonic Professional, Nanoscribe GmbH, Germany) and a proprietary photoresist (IP-L 780, $n = 1.50$ after exposure). The laser writing speed is set to 50 μm/s at 50% laser power. An array of microstructures is fabricated on a glass substrate.
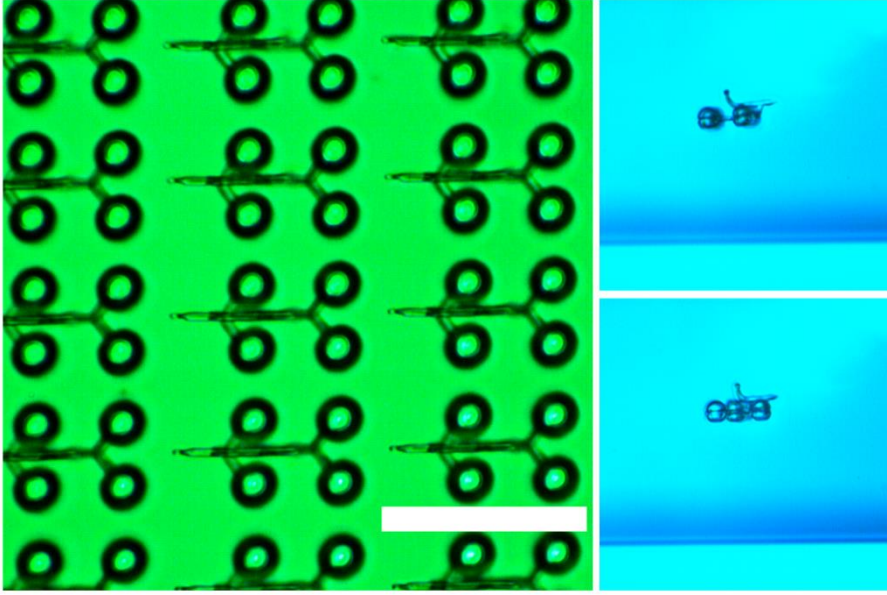
Figure 3.1. Two-photon fabricated wave-guided optical waveguides. Spherical handles are attached to the waveguide structures for optical manipulation. Insets show side-view imaging of an optically manipulated WOW. Scale bar: 40 μm. Image is adapted from [85].

The resulting waveguides have a diameter of $D = 1\,\mu m$ and a bending radius of 6 μm. The surrounding water ($n = 1.33$) serves as the effective cladding for the waveguide and thus the numerical aperture is given by

$$NA = \sqrt{n_{waveguide}^2 - n_{background}^2} = 0.69 \qquad (3.0)$$

The normalized waveguide parameter, V, can be computed using the waveguide diameter, D, numerical aperture, NA, and wavelength, $\lambda = 532$ nm, Substituting the experimental parameters yields a waveguide parameter [87]

$$V = \frac{D\pi}{\lambda} NA = 4.075 \qquad (3.0)$$

For a straight waveguide, the obtained value suggests a multimode operation but because of the small bending radius and the tapering it does not necessarily mean that one will obtain a multimode output. A more detailed analysis of mode propagation in bent waveguide and

effect of tapering can be found in the works of Melloni et al. [88] and Kerttula et al. [89] respectively.

After fabrication, the WOWs are collected by putting a small drop of 0.5% Tween 80 solution with Rhodamine 6G dissolved in ethanol over the structures. The structures are then manually removed and collected by a small capillary tube (Vitrocom, 50 μm × 50 μm inner dimension) attached to a syringe. After collection, the structures are transferred to a cytometry cell (Hellma, 250 μm × 250 μm inner dimensions) where optical manipulation and coupling experiments are performed.

3.2. Optical manipulation of micro-robots

Optical manipulation of the microstructures is done using our Biophotonics Workstation (BWS). A schematic diagram of the BWS is shown in Figure 3.2 and simultaneous manipulation of multiple WOWs is possible with this setup. Counter-propagating beams are used to trap the four sphere handles of each WOW. The arrangement of the handles allows movements with six-degrees of freedom and the axial movement is controlled by changing the intensity ratio of the corresponding counter-propagating beams. The traps are relayed to the sample using two long-working distance objective lenses (Olympus LMPL 50x IR objectives, WD = 6 mm and NA = 0.55). The large working distance allows for side imaging of the sample (Mitutuyo MPlanApo 20x, WD = 20.0 mm, NA = 0.42). Besides showing the trapped structures from another perspective, the side imaging also allows us to image the light emerging from the waveguides when their exit tips face the side camera view. Moreover, by adding fluorescent dye into the trapping fluid, the side imaging provides a convenient method for visualizing the axial propagation of the beams that are diffractively created to address the waveguides.
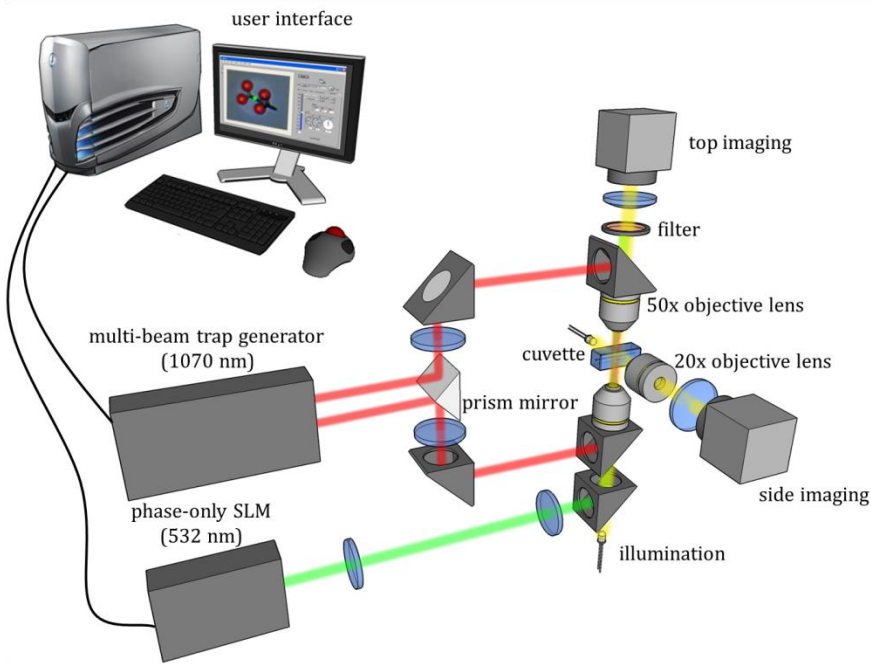
Figure 3.2. The trapping and coupling experiments are performed in our Biophotonics Workstation which uses counter-propagating beams (1070 nm) to hold the spherical handles of the WOWs. A digital holography setup controls the coupling beam (532 nm).

The lateral trapping is limited by the area of the light modulation component and the magnification of the relay optics. The operating area in the sample plane is around 50 μm × 50 μm. The axial trapping is dependent on the ratio of the intensities of the counter-propagating beams. In practice, we can lift a WOW up to a hundred microns from the bottom of the cuvette before toppling over.

3.3. Holographic coupling for 3D light delivery

In order for the WOWs to function effectively in targeted light delivery, the coupling light must be able to follow the WOWs as it move in 3D space. Diffractive approach shows great promise in this regard since it uses phase modulation which uses light efficiently. More importantly, moving the coupling light is straightforward using simple lens and

grating phases. In this section, we discuss the methodology on holographic addressing of the WOWs and show experimental results.

3.3.1. Diffractive addressing workflow

A diffractive SLM-setup has been included to the BWS for the holographic addressing of the WOWs. The main components of the diffractive setup consist of a diode-pump solid-state laser (Laser Quantum Excel, $\lambda = 532$ nm) as the coupling beam and a spatial light modulator (Hamamatsu Photonics, Japan) for phase-only modulation. A simplified diagram of the optical path from the SLM to the camera plane is shown in Figure 3.3. The phase modulated coupling beam passes through a Fourier-transforming lens ($f_1 = 250$ mm). The resulting diffraction pattern is relayed to the sample using a 4f configuration consisting of a lens ($f_2 = 300$ mm) and the bottom objective lens. Imaging is done using the top objective lens and a variable tube lens (f_5). The variable tube lens enables obtaining a focused image of the WOW when it is axially displaced from the imaging plane of the top objective.
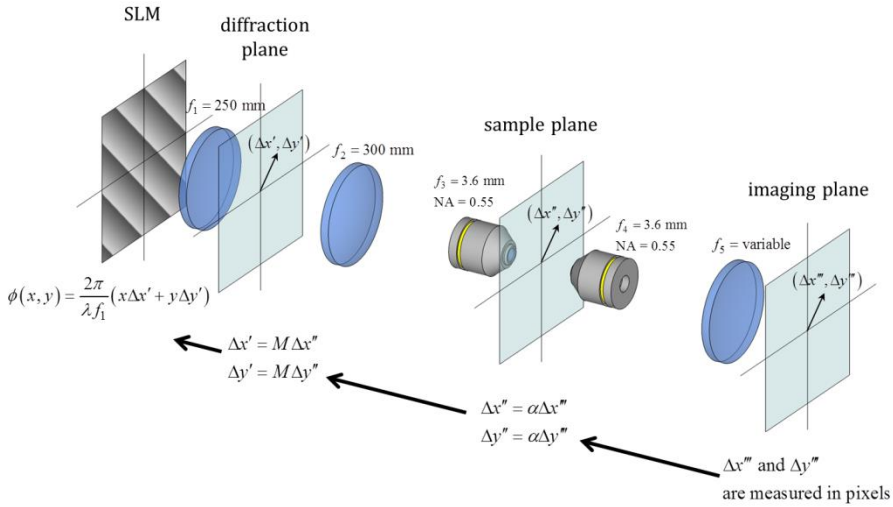

Figure 3.3. Diffractive addressing workflow. The coupling beam passes through different lenses in the Biophotonics Workstation. In order to couple the beam through the waveguide, the magnification needs to be

accounted and the lens and grating phases to be computed accordingly. Image is adapted from [85]

The holographic addressing uses the first diffraction order to couple light through the input facet of each WOW. Since the diffractive setup is independent of the BWS, intermediate calculations and scalings are performed in a separate LabVIEW program having its own user interface. The LabVIEW interface takes the movement of the computer mouse as user input. For ease of control, the interface is overlaid with the acquired video of the sample plane. The mouse movement ($\Delta x''', \Delta y'''$) is measured relative to the position of the zeroth diffraction order in pixels. To get the equivalent physical displacement in the sample plane, a conversion factor α is multiplied to the displacements. This conversion factor is dependent on the focal length of the variable tube lens in the top imaging. The resulting displacements $\Delta x'' = \alpha \Delta x'''$ and $\Delta y'' = \alpha \Delta y'''$ are then magnified with the $4f$ system giving the displacements $\Delta x' = M \Delta x''$ and $\Delta y' = M \Delta y''$ in the diffraction plane. The displacements $\Delta x'$ and $\Delta y'$ now serves as input for the grating phase for lateral movement of the first diffraction order. It is given by

$$\phi_{\text{lateral}}(x, y) = \frac{2\pi}{\lambda f_1}(x\Delta x' + y\Delta y') \tag{3.0}$$

A similar approach is followed for obtaining $\Delta z'$ using the side imaging and its corresponding set of conversion factor and magnification. The axial movement is then controlled using a lens phase given by

$$\phi_{\text{axial}}(x, y) = -\frac{\pi\Delta z'}{\lambda f_1^2}(x^2 + y^2) \tag{3.0}$$

The effect of the grating and lens phase is graphically shown in Figure 3.4. There may be situations where an offset is necessary to minimize unwanted coupling (i.e. from the zeroth order diffraction) or to set a convenient coordinate system for both trapping and coupling. The effective phase for holographic addressing of a single WOW is then given by

$$\phi_{\text{eff}}(x, y) = \text{mod}(\phi_{\text{offset}} + \phi_{\text{lateral}} + \phi_{\text{axial}}, 2\pi) \tag{3.0}$$

The lateral and axial movement of the coupling beam is limited by SLM pixel dimension and the magnification of the $4f$ setup. In the experiment, limitation on the position of the WOW and coupling beam is set by the

BWS since it has a much limited working region. There is also an inherent roll-off of intensity of the coupling beam due to the pixelated nature of the SLM [90].

The interfaces for trapping and coupling are two separate programs. Currently, the positioning of the coupling beam is done manually using a computer mouse and is thus limited by the response time of the user. The refresh rate of the SLM is also a limiting factor which is typically equal to video refresh rate. For real-time tracking and continuous light addressing, passing of coordinate variables and/or video processing is needed between the two programs. This issue is addressed in the succeeding section. The processing time and SLM refresh rate will set the lower operational limit. The latency between trapping and coupling is an important consideration for such a case.
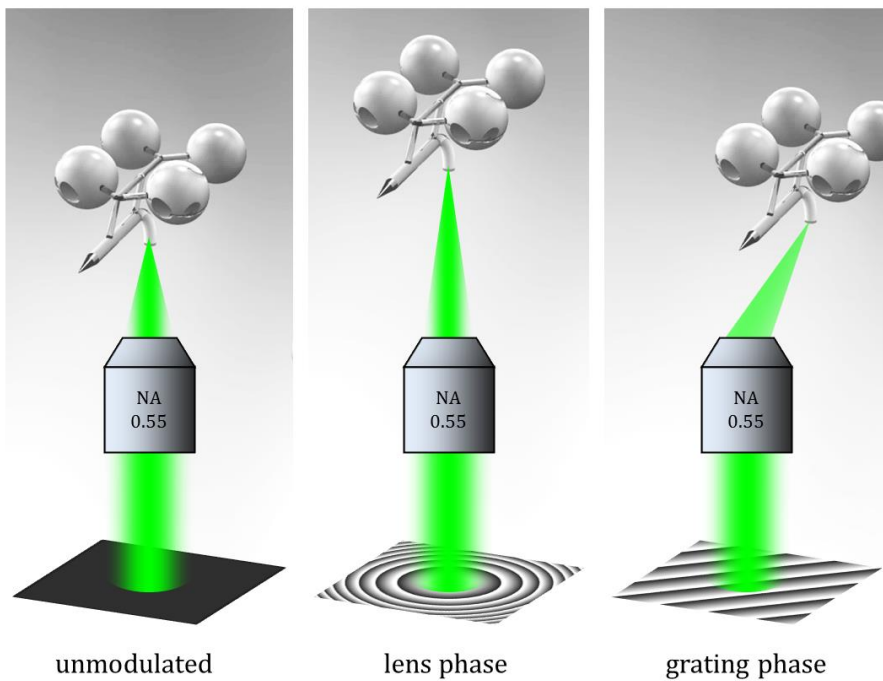

Figure 3.4. Graphical representation of the effect of lens and grating phases. Image is adapted from [85]

For addressing multiple WOWs independently, we may use the random mask encoding technique [91] which uses a disjoint set of randomly selected pixels that is assigned to different WOWs. Each set will therefore have its corresponding grating and quadratic phases. Figure 3.5 shows a snapshot from the side-view microscope, which visualizes the axial propagation profiles of three holographically-created diffraction-limited spots that are focused at different lateral and axial positions. Images such as these can also be used to verify the axial calibration used for encoding phase patterns on the SLM.
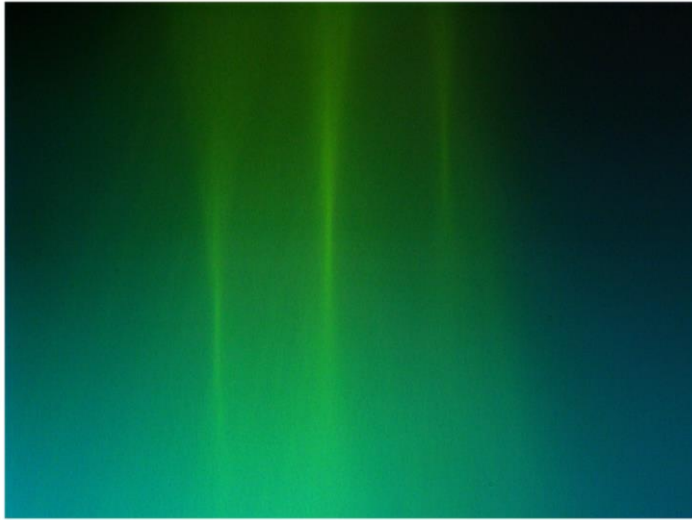

Figure 3.5. The use of holography for coupling the WOWs allows independent control of each coupling beams. Here we show 3 beams at different lateral positions and focused at different depths. Image is adapted from [85].

3.3.2. Light coupling through waveguides manipulated by optical traps

The sphere handles of the WOWs are trapped by counter-propagating NIR-beams for optical manipulation. The coupling beams are focused into the sample chamber upward through the bottom objective. The presence of the coupling beam now limits the degree of freedom of the WOWs into lateral, axial and in-plane rotations. In order to visualize the

path of these coupling beams, a fluorescent dye (Rhodamine 6G in ethanol) has been added to the trapping medium. For the demonstration of light coupling, a single WOW is trapped and rotated such that its tip is facing the side view CCD camera to capture the emerging light. We move the WOW to particular position and use equation 3.5 to get the necessary phase input the will result in a coupling light spot at the position of the input facet. The position of the coupling beam is manually determined using a computer mouse. Once this is set in the coupling interface, the coupling laser is then turned on. This specific and on-demand light targeting implementation is useful, for example, in excitation of specific location and where photobleaching is undesirable. If continuous light addressing is desired, the system can be modified to include a real-time tracking algorithm.

The first part of the experiment is to test coupling for a single WOW as it is being displaced axially within the trapping region. The WOW is displaced axially by changing the intensity ratio of the counter-propagating NIR beams. Figure 3.6 shows a comparison of light coupling with and without holographic addressing.
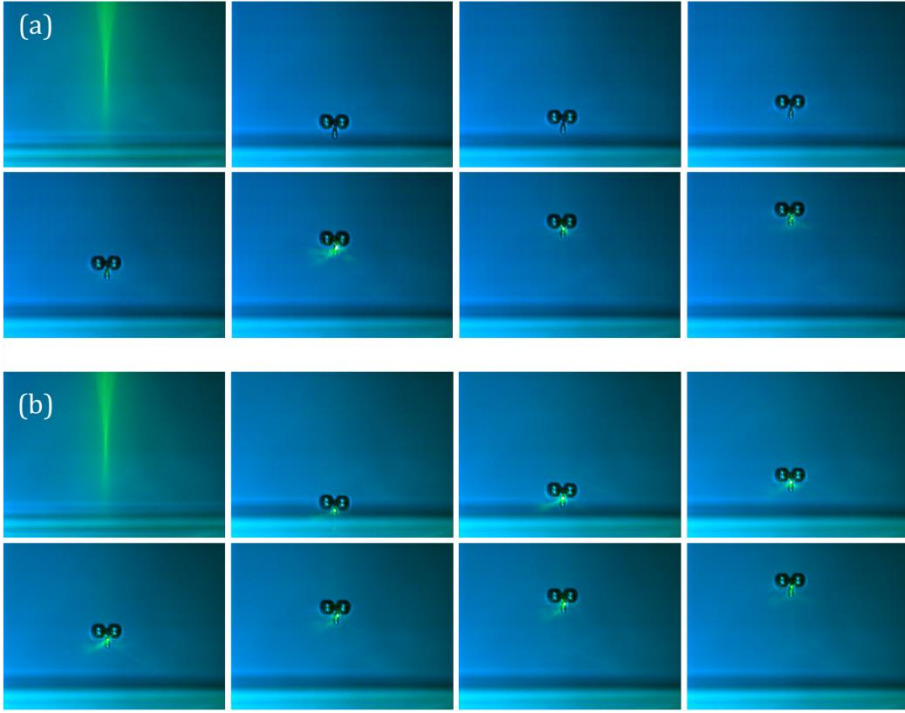
Figure 3.6. Holographic coupling of a WOW being translated axially. (a) Without using the lens phase to adjust the coupling beam, coupling can only occur at certain axial position (i.e. at the objective lens' focal plane). (b) Using a lens phase to adjust the focal position to the input end of the waveguide, the coupling light emerges from the tip at all axial positions. Image is adapted from [85].

Since we are using relatively low NA objectives, the depth of focus of the coupling beams can appear to be relatively large, as shown in Figure 3.5. However, some caution should be exercised when interpreting these side view fluorescence images of the beam propagation since they are not true optical sections and, hence, include contribution from out-of-focus light. Indeed, the range of axial positions that gives rise to significant coupling through the WOW is rather limited, as shown in Figure 3.6a. Thus, a tracking system is required and our results show that the axial range for significant coupling can be extended using diffractive addressing, as shown in Figure 3.6b. The next experimental

demonstration is to test coupling when the WOW is displaced laterally. Figure 3.7 shows a comparison of the lateral coupling with and without holographic addressing.
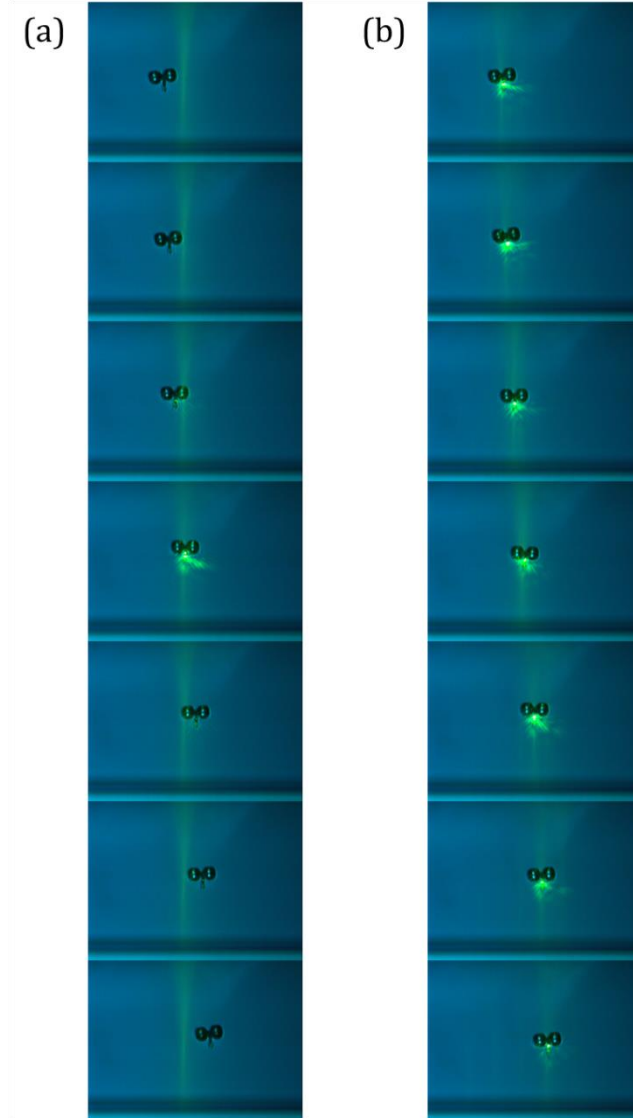

Figure 3.7. Holographic coupling of WOW being translated laterally. (a) Without using the grating phase to adjust the beam, coupling can only occur at certain lateral position. (b) Using a grating phase to adjust the

lateral position of the coupling beam to the input end of the waveguide allow the coupling light to emerge from the tip at all lateral positions. Image is adapted from [85].

Both results for lateral and axial couplings show that a WOW can indeed fully benefit from the dynamic holographic addressing. In contrast to a fixed beam where coupling only occurs at specific points or regions in space, diffractively-addressed WOWs can do full 3D targeted light delivery.

3.4. Summary

We have demonstrated optimal tracking and coupling of wave-guided optical waveguides (WOWs) using dynamic holography for generating beams that track both the lateral and the axial movements of each WOW. The combination of the maneuverability of our waveguides and the dynamic holographic addressing allows full 3D targeted light delivery. This new functionality will prove useful in micro-biological applications such as for photochemical triggering and in nonlinear optics such as nanofocusing. The addition of dynamic holography to the Biophotonics Workstation also opens the possibility of using optimally shaped beams, such as non-diffracting beams for invariant axial addressing of the WOWs. Transverse acceleration of Airy beams can also be used to account for out-of-plane rotations. Airy beams form another class of non-diffracting beams where the main lobe follows a parabolic path during propagation [92]. In contrast to the well-known Bessel beams [93] which uses conical phase in order to generate them holographically, Airy beams uses cubic phase. In the next chapter, we will cover related engineering challenges such as the efficient illumination of the spatial light modulator and real-time tracking of the WOWs.

4.   GPC light shaper for efficient illumination

Our ability to efficiently shape light has paved the way for a host of important progress in photonics and biological research. In the context of this thesis, we have presented holography as an important methodology to targeted light delivery for our light-driven micro-robots. In our specific application, holography is done by modulating the read-out beam with a phase-only spatial light modulator (SLM) to generate dynamic focal spots. Ideally, we want to illuminate the SLM uniformly with a beam that matches the shape of its modulation element (i.e. typically rectangular) as this will utilize much of the pixels in the modulation element. The importance of efficient and uniform illumination becomes clear when we deal with a multitude of micro-robots that all needs to be light-addressed. In general, efficient illumination is always desirable such as in holographic optical tweezers [28,58,94], multi-site two-photon photolysis [95], parallel microfabrication [96], and super resolution imaging [97] and should be encouraged in any optical engineering design.

This chapter will cover the generalized phase contrast (GPC) method for beam shaping as applied to efficient illumination of SLMs. The most common method for illuminating beam shaping devices is expanding and truncating the incident laser beam. While this approach achieves uniform illumination, it sacrifices efficiency by wasting photons. Yet many beam shaping applications demand high efficiency. As an example, the work by Kato et al. [96] on multi-spot parallel microfabrication needed to amplify the laser source to address a fixed microlens array. In this case the available laser power limits the extent to which the process can be parallelized. Since energy is distributed among the focal spots, increasing the number of spots will result in lower intensities for each. More recent example is in super resolution microscopy where there have been reports on 2000-fold parallelized dual color stimulated emission depletion (STED) fluorescence nanoscopy [97]. The lateral resolution of STED nanoscopy is dependent on intensity and therefore such massive parallelization would require high intensity input pulse. Quoting from the authors, "the STED pulse energy is a limiting factor to active highest resolution and large resolved field of view at the same time." The Gaussian envelope of STED intensity makes the resolution position dependent that varies according to square

root law. This particular application highlights the need for high input power and uniform illumination. Power considerations may be mitigated if one can afford high power sources although commercial availability may be difficult for some wavelengths. Given the above constraints, it is therefore necessary to have an efficient photon management system that reshapes light while utilizing as much photons from available laser sources.

The chapter will begin by a brief discussion of the GPC method and then present the GPC light shaper as an add-on module to an existing optical setup. For our purpose the optical setup is exemplified by the holography setup. We will present improvements in output intensities both in an array of focal spots and extended light patterns. Later, this enhancement in the resulting output light pattern is applied to our own light-driven micro-robot for high throughput targeted light delivery.

4.1. GPC light shaper

The GPC method uses a 4f imaging configuration to perform a robust common-path phase-to-intensity mapping as shown in Figure 4.1. The incident Gaussian beam passes through a phase mask that introduces a π phase shift within a defined region. For our purpose we use a phase mask that has a rectangular phase shifting region matching the geometry of the SLM used in the diffractive setup. A lens focuses the beam through a PCF which π-phase-shifts spatial frequencies around the zero-order. A second lens transforms these phase-shifted components forming the SRW at the output of the 4f system. The SRW and the unperturbed copy of the input then interfere at the output plane creating an intensity distribution corresponding to the static phase mask patterns. This creates an intense beam that matches the shape of the phase-only modulation element (i.e. SLM) in the diffractive setup.
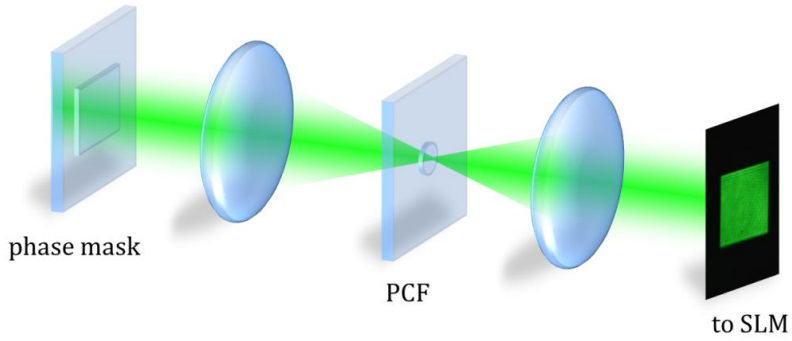
Figure 4.1. Schematic diagram of the GPC Light Shaper. A rectangular phase mask is used to match the shape of the SLM. Image is adapted from [52].

For the experiment, we combine elements of GPC into a compact add-on module called the GPC Light Shaper (LS). Some components can be assembled from off-the-shelf optics parts. The phase masks and phase contrast filters are made from fused silica wafers using wet etching process. The optimal dimension and etch depth of the masks and filters for an input Gaussian beam are previously reported in references [51,98]. Figure 4.2 shows the physical setup for a GPC Light shaper
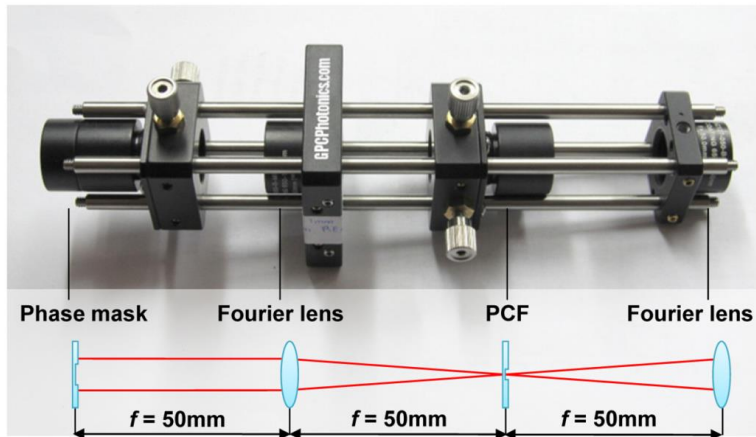

Figure 4.2. An actual GPC Light Shaper prototype. The shaper is constructed from off-the shelf optical components. Image is adapted from [51].

We use a GPC LS designed for $\lambda_0 = 532$ nm wavelength and beam diameter $2w_0 = 1$ mm. A rectangular phase mask with 4:3 aspect ratio is used to match the shape of the SLM. The rectangular phase mask has a width of $W = 2\zeta w_0 = 408.7$ μm and a height of $H = \frac{3}{4}W = 306.5$ μm. The radius of the PCF is given by $\Delta f_r = \eta w_f = 18.76$ μm. The parameter ζ represents the ratio of the phase mask radius and the input beam waist, w_0, while η is the ratio of the PCF radius and the focal beam waist, w_f. For the above calculations, we used the values $\zeta = 0.4087$ and $\eta = 1.1081$ which are optimized for contrast and efficiency [51].

A numerical analysis for a circular phase mask across different η and ζ shows that the acceptable input beam waist can be up to 2.5 times the phase mask radius provided the corresponding PCF is comparable to the beam waist of the focused Gaussian beam at the PCF plane [98]. The limitation on the achievable PCF size is determined by the smallest feature size that can be etched and the damage threshold of the material used since a large input beam would result in a small intense focal spot. Error tolerance calculation for the GPC LS used in the experiment indicate that the system can tolerate axial misalignments within 2% of the focal length of the lens used and lateral displacements within 20% of the PCF radius and still maintain above 80% of its peak operating efficiency [51].

A commercial device known as πShaper also accomplishes this same task using a field mapping approach with a series of refractive elements [99]. The output of the πShaper has high efficiency and has a more flat profile although the output intensity profile is limited to patterns with circular symmetry and a square pattern [100]. The advantage of the GPC LS is that it can work with arbitrary phase mask shapes. The different phase masks and PCFs can be fabricated *en masse* in single fused silica wafer with a standard chemical wet etching process. This makes the GPC LS more economical and moving from different devices is just a matter of changing the appropriate phase mask. A GPC LS designed for λ_0 has also been shown to work with a wide range of wavelength within $[0.75\lambda_0, 1.5\lambda_0]$ [101].

4.2. Enhanced read-out of holograms

For an illustrative SLM-based beam shaping application, we used a diffractive optical setup in an optical Fourier transform geometry, as shown in Figure 4.3, which consists of a diode-pumped solid-state laser (Laser Quantum Excel, $\lambda_0 = 532\,\text{nm}$) with beam diameter $2w_0 = 1\,\text{mm}$. The horizontally polarized laser beam is de-magnified (1/1.5 times) to meet the specifications of the fixed GPC light shaper module which generates a small rectangular output beam profile with a 4:3 aspect ratio. The beam is magnified before passing through a rectangular iris which blocks peripheral light, also allowing direct comparison with a hard-truncated Gaussian. The resulting rectangular beam is then projected to a phase-only spatial light modulator (792 x 600 pixels, 9.9 mm x 7.5 mm active area) to read out holographic phase patterns encoded on the SLM. The modulated beam is Fourier transformed using a lens (f = 250 mm) and subsequently imaged to a beam profiler (Gentec-EO, Beamage 3.0).
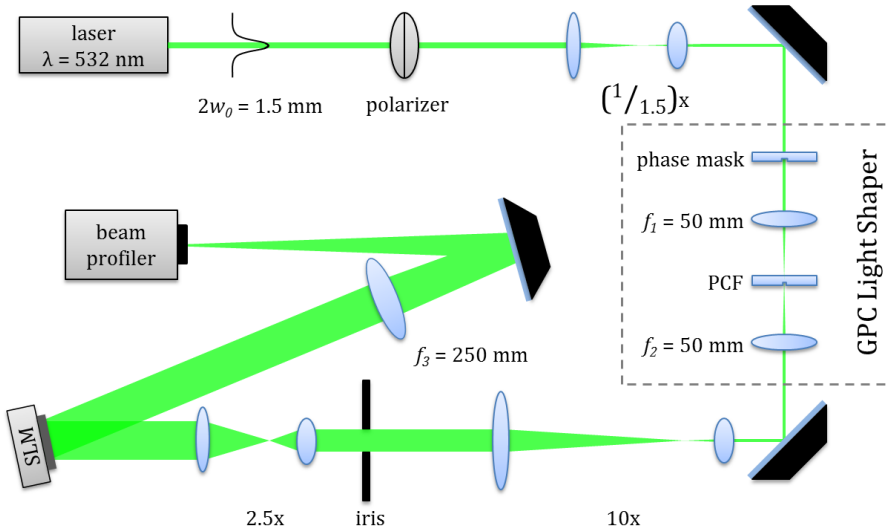

Figure 4.3. Experimental setup for enhanced read-out of holograms. A GPC Light Shaper is added to pre-shape the hologram read-out beam to match the SLM geometry. An iris is added to make a direct comparison with a hard-truncated read-out beam. Image is adapted from [52].

For the hard-truncated input beam, the phase mask and phase contrast filter (PCF) are retained but the PCF is slightly displaced to move the phase shifting region away from the beam path and disable the phase contrast effect. This ensures that the input beam encounters the same material along the optical beam path to the SLM and onwards. During comparison of the GPC-enhanced and hard-truncated hologram read outs, laser power is kept constant. Hence, any improvement is attributed to the beam shaping involved prior to the phase modulation at the SLM.

4.2.1. Gerchberg-Saxton algorithm for phase calculation and intensity distribution synthesis

Our light detectors are only sensitive to intensity and cannot measure phase. One workaround is to use a microlens array to focus an incident wavefront into multiple focal spots. The shifts in the focal spot positions can serve as a measure of the wavefront curvature. This principle is implemented in a device called Shack-Hartmann wavefront sensor. Another method to detect phase or the complex field is to use holography wherein an interference pattern is recorded. A numerical approach uses the propagation equations to calculate the complex field. One such numerical method is proposed by Gerchberg and Saxton in 1972 [102]. The Gerchberg-Saxton (GS) algorithm is originally designed as an alternative phase retrieval method to the more cumbersome hologram recording using interfering waves as originally proposed by Gabor. The GS algorithm calculates the complete field distribution (i.e. amplitude and phase) from intensity recordings along the propagation direction and relies on the propagation relation between the planes. The algorithm iterates between the intensity planes where the recorded intensity patterns are converted to amplitude and imposed as constraints while keeping the phase information throughout. The goal is to arrive at a self-consistent complex field that matches the intensity recordings at their respective planes upon propagation. In this respect, the GS algorithm can be thought of as an error reduction algorithm where the difference in the recorded intensity and the generated intensity from the iteration is minimized. An error criterion such as normalized mean square error (NMSE) can be used as stopping condition for the GS algorithm and the phase for the complex field

distribution can be retrieved. More details on iterative phase retrieval algorithms can be found in literature [103–106].

Aside from phase retrieval from existing intensity distributions, the GS algorithm can be used for synthesis of light intensity distributions. Here, we create our desired intensity distribution and calculate the phase that will result to it. The calculated phase will serve as input for the SLM that will modulate an incident beam. In this application, we are essentially engineering light to behave in a manner that we want. However, we are still bounded by the limits set out by the physical system we are using. For example, SLM's are planar devices and thus makes 2D mapping. To generate 3D output light field distributions, one can make use of multi-plane GS algorithm or multiplexing but the result suffers from intensity crosstalk between the planes [107–109]. Alternatively, using an Ewald sphere representation for the spatial frequencies and subsequently mapping to a 2D SLM can be used to create physically realizable 3D intensity distribution. This approach uses 3D Fourier transform and may take considerable time for a convergence of solution [110,111]. The Fast Fourier transform implementation on modern computers and/or graphics processing units can be used for faster calculation and larger array sizes.

Here we discuss an adaptive GS algorithm for intensity distribution synthesis [112]. Consider two planes, one for the source plane and another for the image plane. These planes are on the back and front focal plane of a lens respectively and thus have a Fourier transform relation. The algorithm is shown in Figure 4.4. The implementation of the GS algorithm may start with an initial phase (e.g. a random phase distribution) and a source amplitude constraint such as the rectangular profile from the GPC LS which also serves as the hologram read-out beam. The complex field $E_n'(x,y) = A_{laser}exp(i\varphi_0)$ is Fourier transformed to simulate the function of the lens and results in $E_n(u,v) = A_n \exp(i\varphi_n)$. The subscript n serves as iteration counter. The obtained amplitude $A_n(u,v)$ is compared to the desired amplitude $A_{desired}(u,v)$ by means of NMSE. If a set error threshold is not met, a modified target amplitude $A_n'(u,v)$ is

calculated using a weighing function. The modified target amplitude is given by [32]

$$A_n'(u,v) = A_{n-1}'(u,v)\left[\frac{A_{desired}(u,v)^2}{A_n(u,v)^2}N_n\right]^{\gamma} \tag{4.1}$$

where N_n is a normalization parameter given by

$$N_n = \frac{\sum\limits_{u,v} A_{n-1}(u,v)^2}{\sum\limits_{u,v} A_{desired}(u,v)^2} \tag{4.2}$$

and γ is a gain parameter which we set to 0.5 throughout in this chapter. The resulting field $E_n'(u,v) = A_n'\exp(i\varphi_n)$ is back-propagated to the source plane to get $E_n(x,y) = A_n\exp(i\varphi_n)$. The amplitude $A_n(x,y)$ is discarded and replaced with $A_{laser}(x,y)$ for the next iteration. If the error is below a threshold, the algorithm stops and the phase $\varphi_n(x,y)$ is the optimized phase that will result in the desired amplitude. The use of an adaptive algorithm ensures uniformity in the output intensity patterns. The adaptive GS algorithm is used to calculate the optimized phase to generate random arrangement of focal spots and extended intensity patterns.
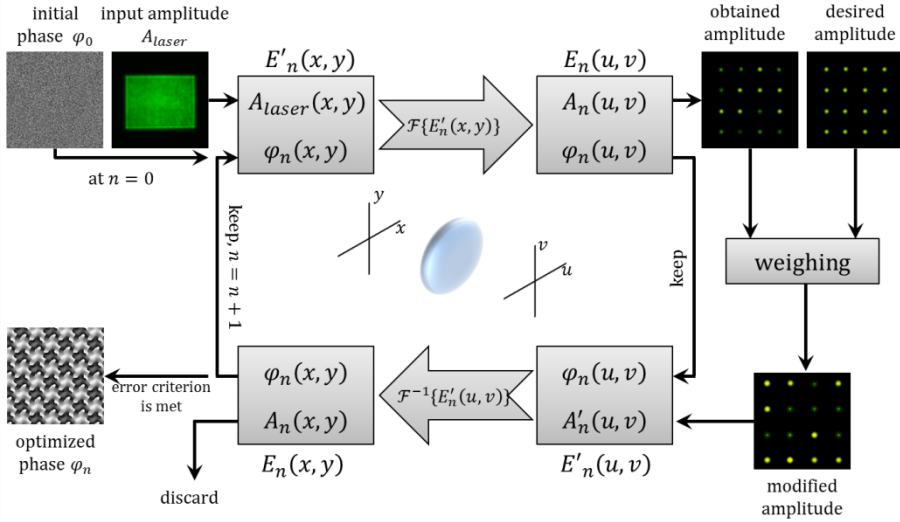
Figure 4.4. Adaptive Gerchberg-Saxton algorithm with spatially varying weighing function. Image is adapted from [112].

4.2.2. Intensity increase and phase flatness of hologram read-out beam

Comparison of the intensity of the read-out beams shows that GPC-enhanced beam (see Figure 4.5a) has approximately three times brighter than with its hard-truncated counterpart (see Figure 4.5b). Note that the incident laser power is kept constant for each case. The phase flatness of the read-out beam is an important consideration in digital holography. Ideally, the read-out beam should have a flat phase to avoid any aberration or at least the phase should be known so that it can be included in the iterative algorithm or to allow compensation in the SLM.

To get the phase profile of the GPC-enhanced and the hard-truncated beam read-out beam, a multi-plane phase retrieval algorithm is used based on the Gerchberg-Saxton algorithm [102]. Four images separated by 1 mm are taken by imaging the beam emerging from the iris to the beam profiler. These intensity images serve as amplitude constraints in the calculation. The normalized mean square errors for the iterative calculations are below 0.002. The phase is flat for both beam shaping modalities within the high intensity region as shown in Figure 4.5c for the GPC-enhanced and Figure 4.5d for the hard-truncated. Abrupt phase change happens at the edge of the rectangular intensity pattern. The line scans for the phase show rapid fluctuations outside the region of interest due the dark noise from the beam profiler, but this is not critical for the application.
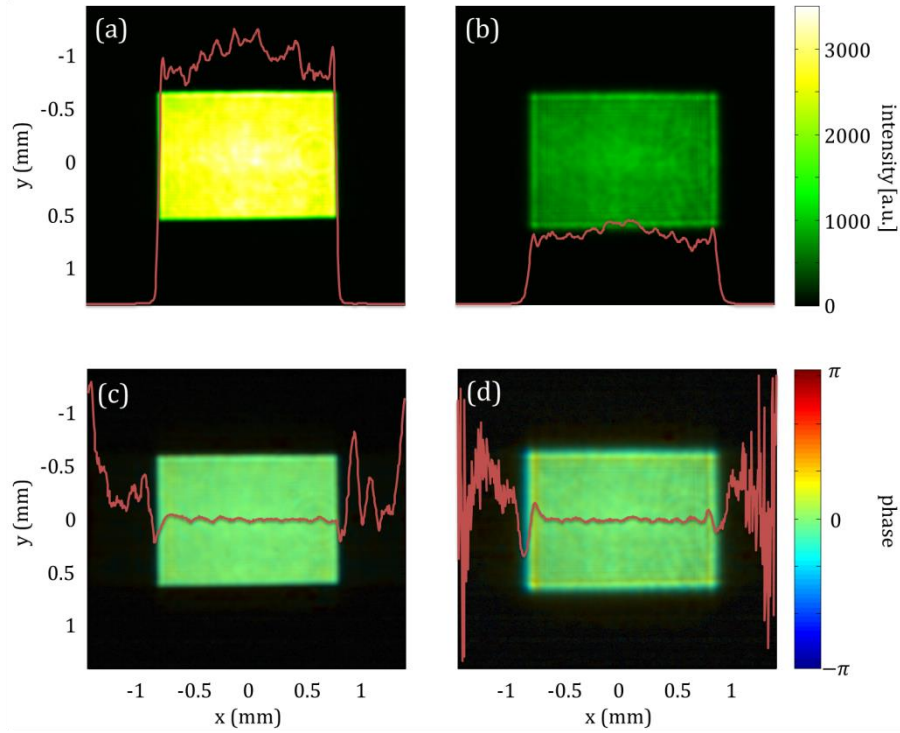
Figure 4.5. Comparison of the GPC-enhanced and hard-truncated read-out beam. The intensity of the (a) GPC-enhanced beam is higher compared to the (b) hard-truncated beam. The phase is flat for the (c) GPC-enhanced and (d) hard-truncated. Line plots are taken at $y = 0$. Image is adapted from [52].

There are other applications where a circular input is desired such as in direct illumination of microscope objective for fixed beam optical trap. The GPC LS can also adapt a circular shape and other rectangular shapes by simply changing the phase mask as shown in Figure 4.6.
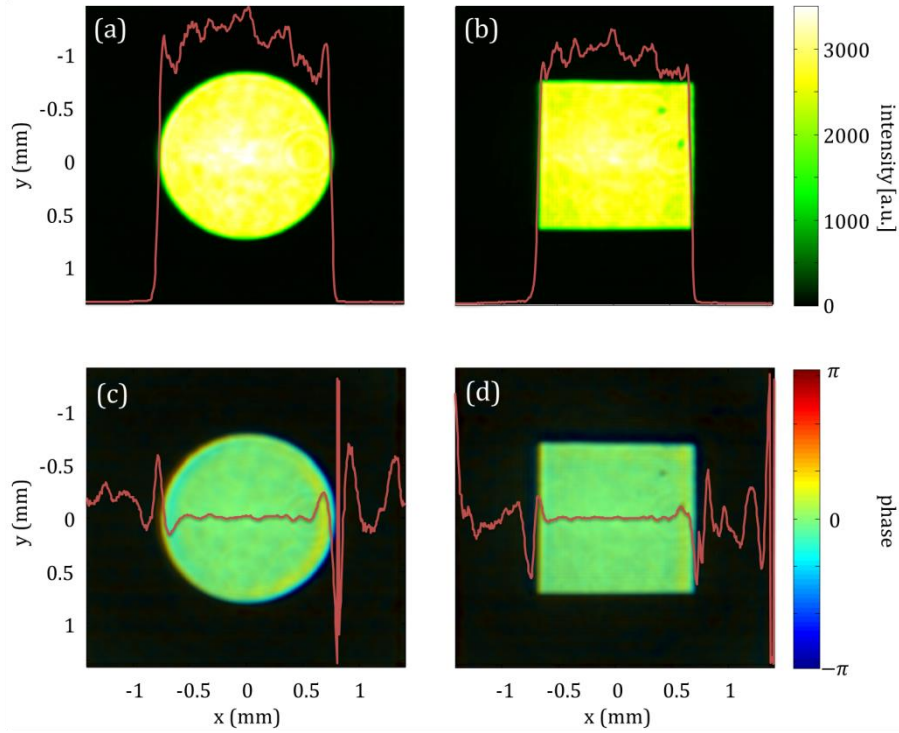
Figure 4.6. Different hologram read-out beams can be used by simply changing the phase mask of the GPC LS such as (a) circle and (b) square. The phase profiles for each shape are shown in (c) and (d) respectively. Image is adapted from [52].

4.2.3. Comparison of hologram reconstruction

Typical applications of diffractive phase modulation are for light-efficient dynamic spot generation in optical tweezers or, more recently, for uncaging neurotransmitters and optogenetic photoexcitation in neurophotonics research. Hence, we first tested the GPC light shaper in a dynamic spot-projecting holographic configuration. We performed an adaptive Gerchberg-Saxton algorithm as described in the preceding section to compute the phase pattern necessary for generating a random arrangement of light spots. We have, however, not optimized the phase to produce patterns with a reduced zero-order and/or higher-order spurious diffraction. Holographic projections were demonstrated for both GPC-shaped and for hard-truncated input beams. The GPC-

enhanced spots are more intense than their hard-truncated counterparts and do not exhibit any gross distortions, consistent with expectations from having a flat phase determined earlier. The intensity gain is quantified using the ratio of the average light spot intensity in the GPC-enhanced pattern to the corresponding average light spot intensity in hard-truncated case. The zero order diffraction is not included in the calculation.
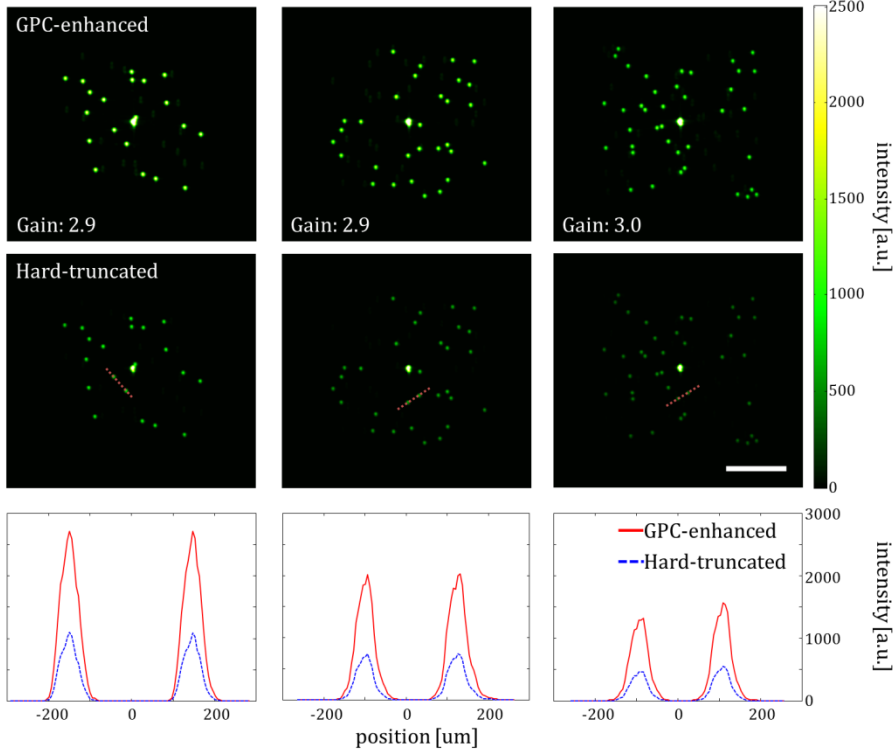

Figure 4.7. Intensity distribution of randomly arranged focal spots. The GPC-enhanced spots are much brighter as evident in the line scans. The gain is calculated for each distribution. Scale bar: 1 mm. Image is adapted from [52].

Both the GPC-enhanced and hard-truncated read-out beams have flat phase making them suitable for phase modulation applications. However, the high intensity gain from the GPC-enhanced beam has major advantage for many applications. Figure 4.7 clearly shows a

significant increase in the intensity of the generated spot arrays when using GPC-enhanced read-out. The ~3x gain means that three times more intense spots can be holographically generated with a GPC-enhanced read-out using the same incident laser power. Alternatively, this enables a user to generate an array with 3x more spots having the same intensities as the fewer spots when reading out by a hard-truncated beam. For example, the 40 spots created by GPC-enhanced read-out in are still brighter than the 20 spots in the hard-truncated case. This new functionality could have a large impact for various applications, e.g. requiring multiple optical tweezers [94], multi-site two-photon photolysis [95] and in parallel two-photon polymerization [96].

Another typical holographic application is the generation of arbitrary extended intensity patterns. However, the inherent presence of speckles is one major drawback of this beam shaping technique. A major cause of speckles in diffractively-generated extended light patterns is the "randomly" oscillating phase distribution at the far-field reconstruction plane mainly caused by cross-talk between adjacent output resolution elements due to the optical convolution process with the point spread function (PSF) of the system [90,113]. Considering that we get 4:3 rectangular output with both GPC LS and hard truncation, the PSF for both will have a 2D sinc profile matching the 4:3 aspect ratio and the difference will only be by a scaling factor due to the gain in the GPC LS. Alternatively, the SLM can be illuminated directly with small Gaussian beam to fit inside the active phase modulation region. However, this comes at the expense of losing some of modulation pixels and consequently having a broader jinc PSF. Moreover, the central hotspot can be problematic for high power applications, as previously discussed at the beginning of this chapter, which provides the motivation for using uniform illumination. Utilizing much of the SLM pixels is suggested for applications requiring finer resolutions and thus highlights the importance of a properly match read-out beam.

For our extended pattern targets, we use the university's logo and a binarized version of a standard test image. Figure 4.8 shows our results for extended light patterns and there is a substantial intensity gain in the resulting holographic reconstruction of extended intensity patterns

similar to the spot arrays. The presence of speckle is in general an undesirable feature of phase-only holography but for some applications this can be tolerated when the aim is to efficiently generate high intensities such as is the case for two-photon fabrication [114,115].
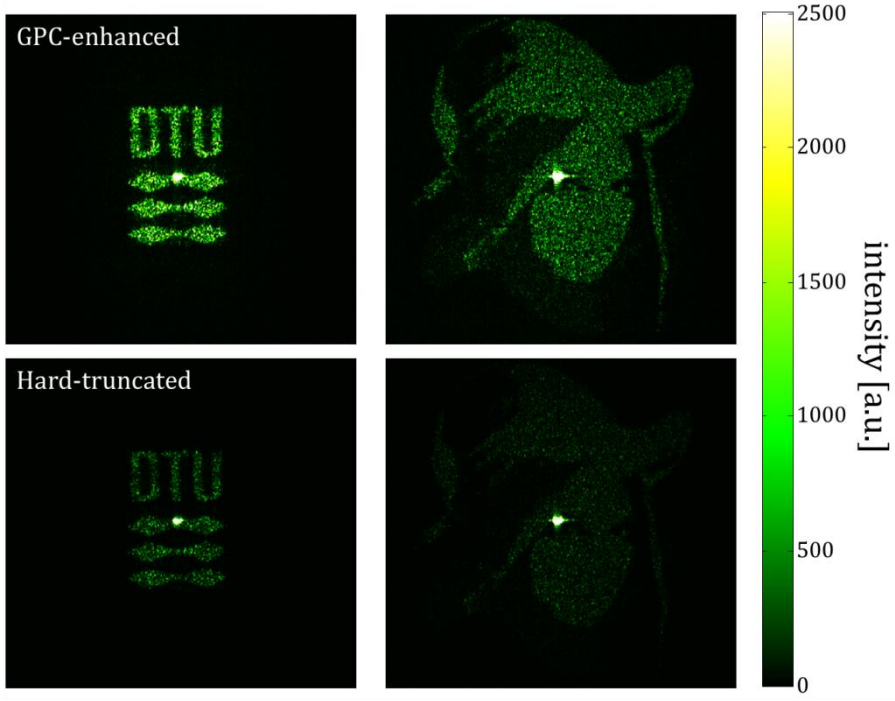

Figure 4.8. Intensity distribution of extended patterns using GPC-enhanced and hard-truncated read-out beams. Image is adapted from [52].

Complex beam shaping methods may be employed to reduce speckles however cascading SLMs or other pixel-based diffractive modulation element to address both amplitude and phase is inefficient due to the inherently low diffraction efficiency of SLMs and may demand high input powers for operation. Typical efficiency of the first diffraction order from a phase grating in an SLM is 40.5%.

4.3. Enhanced coupling to wave-guided optical waveguides

As an application of this hologram read-out enhancement, we added the GPC light shaper in our holography setup for dynamic coupling of the WOWs introduced in the previous chapter. We have also implemented an object tracking algorithm to automatically retrieve the position of the WOWs and calculate the necessary phase for the coupling light. This combination of efficient and real-time coupling significantly leverages the capabilities of our WOWs for potential application in photostimulation and to initiate nonlinear optical phenomenon on tiny scales.

4.3.1. Object-tracking algorithm for real-time light delivery

As, before, the WOWs are manipulated using the spherical handles held by the counter-propagating trapping beams (λ_{trap} = 1070 nm). In this scenario, a lateral movement of a single micro-robot can be accomplished by simply dragging the beams along the lateral direction. The axial movement can be performed by changing the intensity ratio of the trapping beams. As the WOW moves in 3D space, we require its coupling beam (λ_{coup} = 532 nm) to track and follow it for continuous addressing. The lateral displacements $\Delta x'$ and $\Delta y'$ of each micro-robot can be readily obtained from the trapping interface since the trapping beams uses an imaging geometry and thus only a simple scaling is needed for the hologram calculations. The axial coordinate cannot be inferred directly due to the counter propagating nature of the trapping beams. Hence, we need to use an object tracking routine on the side-view imaging to automatically get the axial displacement parameter $\Delta z'$. The built-in tracking routine in LabVIEW uses the mean shift algorithm. It is a non-parametric iterative algorithm used in pattern recognition and computer vision [116,117]. The algorithm is able to determine the position of the micro-robot at video frame rate. The setup and procedure is summarized in Figure 4.9.
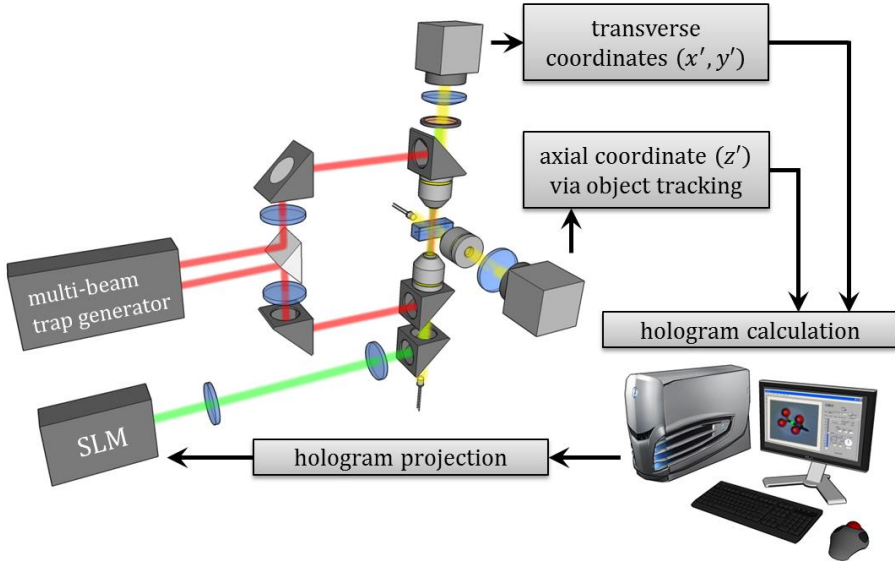
Figure 4.9. Schematic diagram of real-time enhanced coupling experiment. Image is adapted from [86].

The required phase holograms for the lateral and axial movements of each coupling beam are calculated using the lens and grating phases as described in equation 3.5.

4.3.2. Color-based image segmentation for data processing

A long pass filter with cutoff wavelength at 550 nm is placed before the applied CMOS camera to remove the coupling beams and use the fluorescence signal to measure the total power output at the tip of the micro-robot. We use an image segmentation approach based on the color channel of the captured images to ensure that we compute only the fluorescence signal. We take advantage of the RGB color model used to represent the captured images. The RGB color model is an additive model where different colors are produce by mixing three primaries (i.e. red, green and blue) [118]. A cyan filter is installed with the white LED for the side illumination. The resulting cyan color illumination registers in the CMOS camera as having a RGB value of (0, 255, 255). The micro-robots are practically transparent and also appear as cyan except for the edges. Thus, the greenish fluorescence signal will result in localized variations in the red channel only. Figure 4.10 shows a particularly good localization of the fluorescence signal at the tip of the micro-robot.

Furthermore, we can calculate the "center of mass" from the red channel data to pinpoint the location of the tip and integrate the total power within the vicinity. This procedure is similar to tracking fluorescent low density lipoprotein receptor molecules [119].
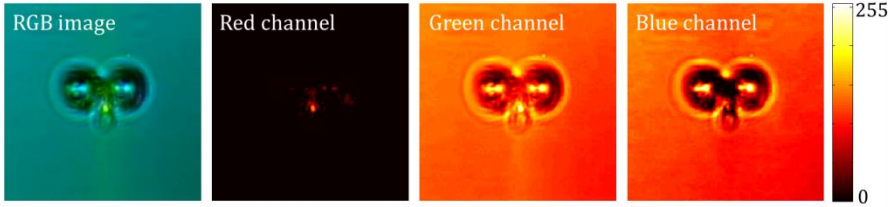

Figure 4.10. Image segmentation based on color channel. The red channel shows a good localization of the fluorescence signal. Image is adapted from [86].

4.3.3. Brownian motion of trapped micro-robot

Crucial to optimal coupling is to account for the uncontrolled movement of the trapped microstructures due to Brownian motions. We measure the amount of fluctuations of each micro-robot by trapping it in a fixed position and use the output coupling beam at the tip as a light beacon to locate its position. The trajectories for both GPC-enhanced and hard-truncated coupling beams are plotted in Figure 4.11a and Figure 4.11b respectively.
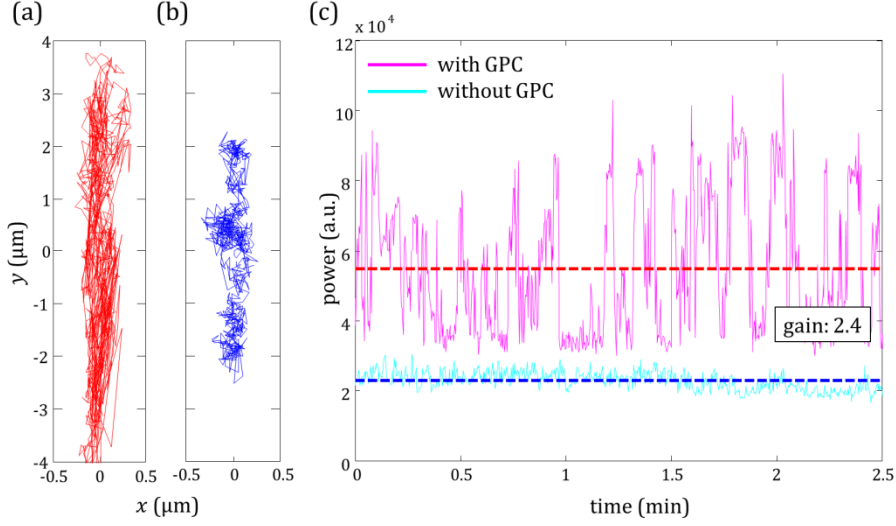
Figure 4.11. Comparison of Brownian motion of trapped micro-robots with (a) GPC-enhanced and (b) hard-truncated coupling beams. (c) Power outputs of the micro-robots with different coupling. The dashed line shows the average power value. Image is adapted from [86].

In both coupling cases, there is a small movement along the lateral direction but a large variance along the axial direction. This is due to the relatively weak axial confinement obtained by low-NA counter-propagating beam traps. However, there are more pronounced fluctuations in the GPC-enhanced coupled micro-robot. We attribute this to the stronger recoil of the structure from the more intense coupling beam [47]. This effect can be minimized by modifying the shape of the handles [42,43]. Figure 4.11c shows the output power fluctuations for the duration of our observation. We took the average power for both coupling cases and took the ratio to calculate the gain. We found the value to be 2.4 for a GPC-enhanced coupled micro-robot.

4.3.4. Real-time coupling of wave-guided optical waveguide

Coupling has been tested for both lateral and axial displacements of the micro-robots, separately. The lateral movement is performed by dragging its associated trap using a computer interface. The coordinate variables are then grabbed to calculate the required grating phase. For

axial coupling, the position of a micro-robot is obtained from the built-in object tracking routine in LabVIEW. The obtained axial displacement is then used to calculate the required lens phase. The results for the lateral and axial coupling are shown in Figure 4.12a andFigure **4.12**b respectively. The total power for each case is calculated frame by frame for the duration of the observations (~6 seconds) and the average power for each coupling case is taken to compute the gain.
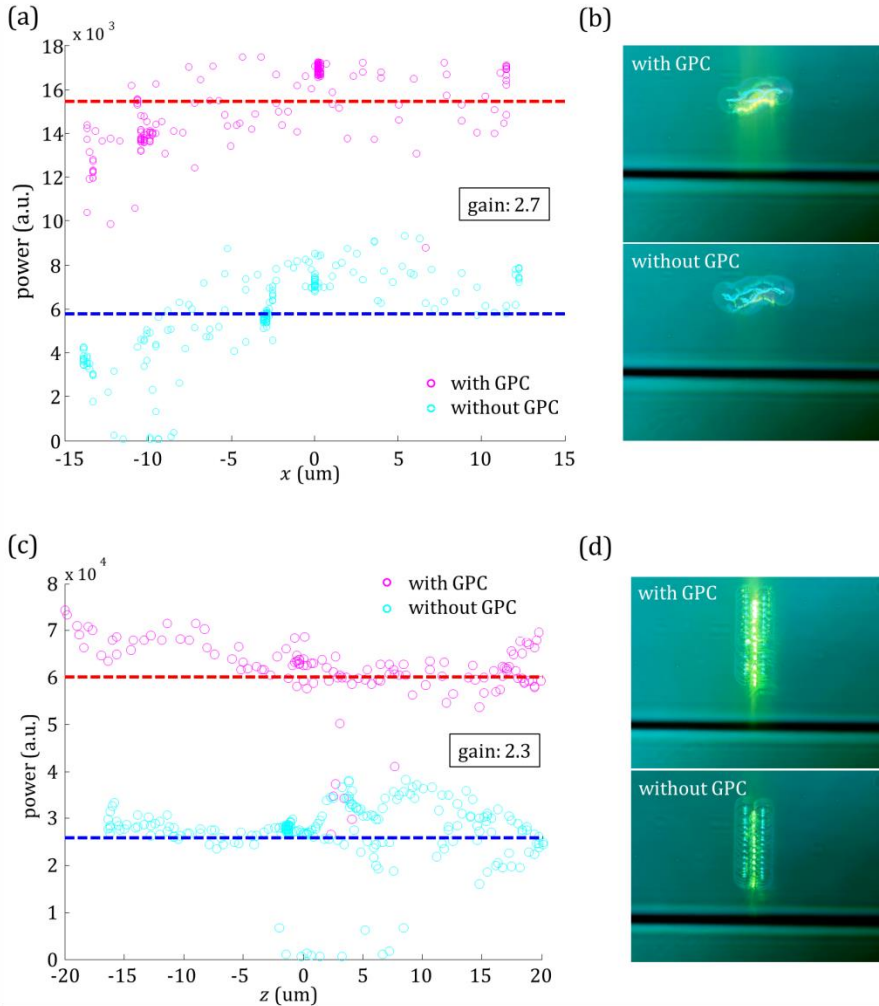

Figure 4.12. Power variations of micro-robots as they are moved (a) laterally and (c) axially. The dashed lines represent average power values. (b) and (d) show the

trace of the micro-robots' movements as they are manipulated and holographically coupled laterally and axially respectively. Image is adapted from [86].

In both lateral and axial coupling experiments, the GPC-enhanced coupled micro-robots show the highest total output power. This boost in output tip-light from the micro-robots can have potential applications when the aim is to trigger nonlinear light phenomena in biological samples. The micro-robots can be coated with gold nanoparticles to trigger local field enhancement for better fluorescence signal [45]. In Figure 4.13, we demonstrate coupling following an arbitrary path.
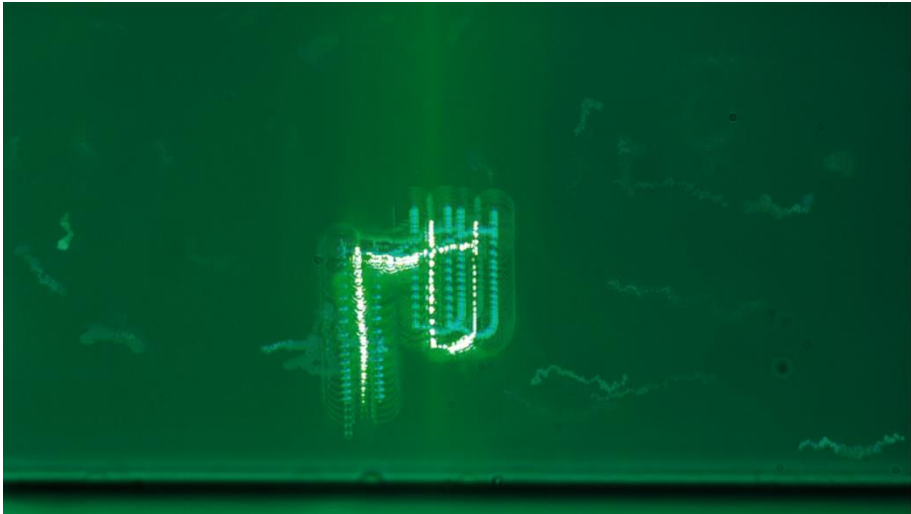

Figure 4.13. Demonstration of GPC-enhanced real-time coupling of an optically manipulated WOW following an arbitrary path. Image is adapted from [86].

4.4. Summary

We have presented a light-efficient method of reading out a phase-only spatial light modulator using the Generalized Phase Contrast method as a compact add-on module called the GPC Light Shaper. The method utilizes as many photons as possible in a given laser power setting creating a high intensity output that matches the shape of the modulating device. The flat output phase makes it suitable for illuminating phase-only spatial light modulators. We have shown the ability to create trapping spots or diffractive light patterns that are

about 3 times more intense than using the traditional approach of hard-truncation. Alternatively, this means we only need 1/3 of the laser power to create similar intensity-level patterns to the hard-truncated case or 3 times more trapping spots or diffractive pattern fill factor.

The above conclusion can be appreciated better when one considers a scenario where a given laser source is already operating at its maximum output and yet still not sufficient to perform, for example, a holographic multi-beam trapping experiment of colloidal particles. The use of the GPC LS prior to holographic encoding is able to "squeeze out" 3 times more photons compared to the simple hard truncation. This gain in photons might just allow an experimentalist to carry out this trapping experiment with the given maximum power at hand. This scenario can be extended to application cases that aim to parallelize processes based on focused light by producing multiple foci.

The method presented here can be advantageous for a host of photonic applications such as multiple optical tweezers, multi-site photolysis in neurophotonics and parallel two-photon polymerization. Moreover, multiple plane beam shaping techniques can benefit from this enhanced read-out since the static beam shaping using the GPC LS is independent of the reconfigurable SLM phase encoding. Due to the versatility of the input phase masks for the GPC LS, the system is not limited to just simple rectangular or circular apertures of basic light modulating elements. For example, the phase masks used in the GPC light shaper can also be fabricated for systems requiring a light-efficient read-out of e.g. a microlens array or photonic devices with inherent specifically shaped active modulating elements.

As an application of the enhanced hologram read-out, we have experimentally demonstrated real-time continuous coupling of green laser light to near-infrared laser-trapped and manipulated micro-robot, the WOWs, by using an object tracking algorithm. The addition of our GPC Light Shaper in the diffractive setup allows for an efficient formation of high intensity light spots that are particularly suitable when addressing a plurality of moving micro-robots simultaneously. We have obtained an output gain of up to 2.7 times and this complements well with the targeted-light delivery capability of the micro-robots. The

ability to switch between on-demand and continuous high intensity coupling offers versatility for the light-guiding micro-robots for potential applications in photo-stimulation and near-field excited nonlinear optics.

5.   Light micro-robotics for material transport

We have presented so far the use of light to impart momentum on polymerized microstructures to move them around. In this chapter we present a new generation of light-driven micro-robots with a novel and disruptive functionality. The purpose of the new micro-robots is to transport cargo and it is designed to be self-contained. The mechanism to load and unload cargo is built-in within the micro-robot. Inside the micro-robots are thin metal layers that are heated with a laser beam to generate secondary hydrodynamic effects such as thermal convection and microbubble to draw cargo in and out of the structures.

This chapter starts by discussing the fabrication process for this new type of micro-robot as well as the challenges along the way that resulted in its current design. We will demonstrate loading and unloading experiments that show promise in material transport. We will end this chapter with a discussion on the implication of these results in the field of drug delivery and as potential vehicle for plasmonics.

5.1. Design and fabrication of the transport vessel

As we have discussed earlier, a good micro-robot should have all its parts built-in. In this section we will discuss the fabrication of optically actuated micro-robot for material transport. The body of the micro-robot is hollow to serve as container. We have tried different designs and take into consideration the loading and unloading mechanism. We have come up with a micro-robot that utilizes photothermal heating of an embedded thin metal layer to generate convection current that draws in and out the cargo.

5.1.1. Fabrication of hollow structure: Initial design

Our fabricated micro-robots are designed to act as a vessel for material transport and thus should have an opening for loading and unloading of cargo, a hollow body for storing the cargo and handles for optical manipulation. For the initial investigation of this concept, we choose a simple ellipsoid with axes having lengths of 20 um, 8 um and 8 um and therefore has a volume of around 5 picoliters. We have tried different diameters for the opening of the micro-robot. For the experiments and results presented here, we use around 2 um hole on both end of the ellipsoid. The micro-robots are fabricated with two-photon process as

with the WOWs. A brightfield and scanning electron microscope (SEM) image of the structures are shown in Figure 5.1. The structures are fabricated on a microscope cover slip.
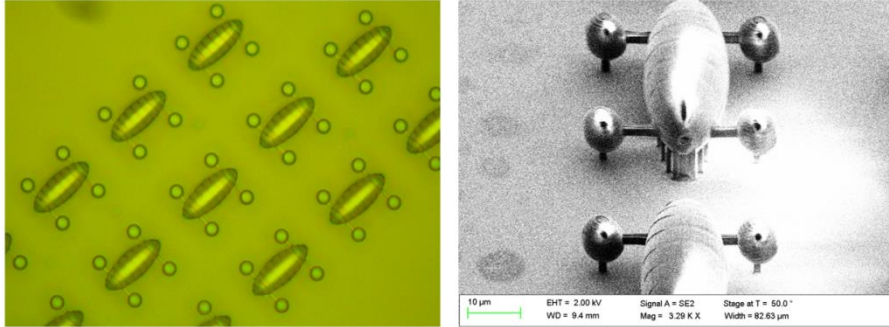

Figure 5.1. Brightfield and SEM images of two-photon fabricated micro-robots. The body of each micro-robots is hollow with only small openings for loading and unloading of cargo. Image is adapted from [120].

5.1.2. Light-controlled loading and unloading: Early demonstration

To test if the structures are indeed hollow as intended, we put a few drops of deionized water over the structures. As the water slowly engulfs the structures, we see some trapped bubbles inside the ellipsoid indicating that they are hollow. It takes some time for the water to get inside the structures through the holes and for the bubbles to disappear. While there is still a bubble inside a micro-robot, we tried placing a trapping beam on one end of the structure and we observed that the trapped bubble moves toward the beam (see Figure 5.2). This phenomenon is called thermocapillary bubble migration which is a consequence of the temperature-dependent surface tension gradient in the air-water interface [121]. This suggests the possibility of using a trapped bubble as pump as was demonstrated in microfluidics [122]. In the later sections, we will show an improvement of the design of the micro-robot and a more in-depth discussion on this phenomenon.
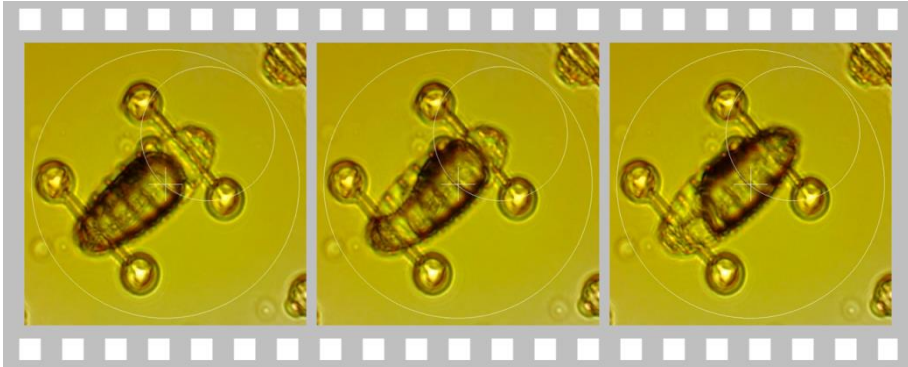
Figure 5.2. Thermocapillary bubble migration inside the micro-robot. The bubble is attracted to the trapping beam marked by the smaller white circle. Image is adapted from [120].

As an initial attempt to verify this possibility we add a solution containing 1 um polystyrene beads on the structures and load them inside the micro-robot. Using a trapping beam from a 1070 nm laser, we control the bubble inside to imitate a pumping action. The experimental result shown in Figure 5.3 demonstrates that beads can be loaded inside. In a similar manner, the beads can be pumped out by placing the beam in the other end of the structure.
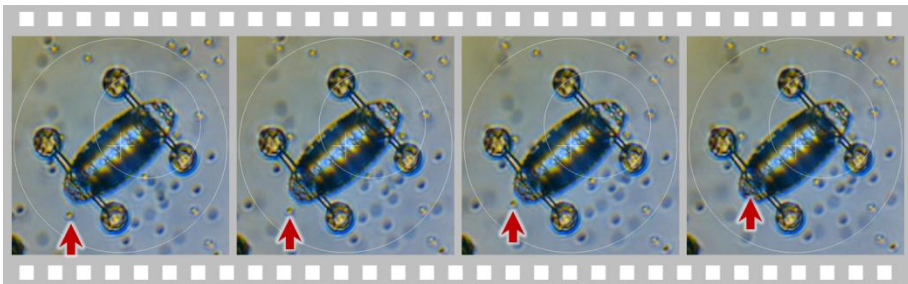

Figure 5.3. Loading of beads inside the micro-robot using thermocapillary bubble migration. Image is adapted from [120].

5.1.3. Embedding a metal layer inside the micro-robot

The loading and unloading mechanism in the preceding section has been demonstrated with the structures still attached to the glass substrate and with a trapped bubble still present. However, for trapping

experiments and especially with *in vivo* applications, the micro-robots need to be optically manipulated and the loading/unloading mechanism should be reliable. In other words, it should be self-contained. The challenge with a trapped micro-robot is that it is quite difficult to induce bubble formation or even thermal convection due to the low absorption of the polymer comprising the structure and also the trapping medium. Our solution is to embed a thin metal layer inside the structure that has high absorption with the trapping beam. To test whether this approach will work, we first deposited a thin metal layer on microscope coverslip and shine a 1070 nm beam. We use electron beam physical vapor deposition method to cover the glass substrate. The deposited metal layer consists of 1 nm titanium as adhesion layer and 5 nm layer of gold. We have observed bubble formation and strong thermal convection starting at 17mW laser power as shown in Figure 5.4. We have also observed strong convection current within the vicinity of the bubble. Earlier work based on similar phenomenon using plasmonics has shown applications in fluid mixing [123], thermoplasmonics [124], optofluidic control using photothermal nanoparticles [125] and micropatterning [126]. Numerical simulations on heating plasmonic structures show that convection current can be formed around them and thus allows the possibility to control fluid flow [127]. In this thesis, however, we did not investigate further if we are observing plasmonics.
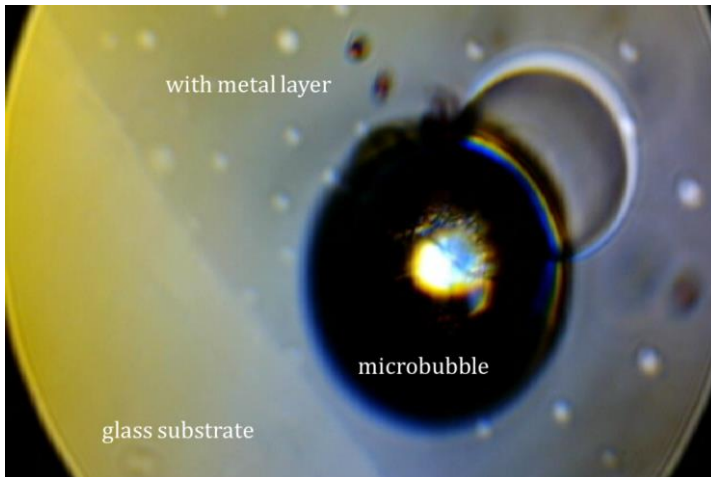

Figure 5.4. Heating of thin metal layer on glass substrate using a 1070 nm counter-propagating trap. The thin

metal layer consists of 1 nm titanium adhesion layer and
5 nm gold thick gold layer. Image is adapted from [120].

The result we got from the thin metal layer on a glass substrate is encouraging. Thus, the next step is to place the metal layer inside the structure. For this part, the challenge now is how to expose only the region where the metal layer is to be deposited while protecting the rest of the structure. To solve this, the ellipsoid body of the micro-robot has been changed to a different design.

The shape of the new micro-robot is based on the surface of revolution of the so-called teardrop curve [128,129]. Cargo may be loaded and unloaded through an opening at the anterior part of the structure. The diameter of the spout is set to 6 μm. Spherical handles are added to the structure for optical trapping and manipulation. A hole is left open on top of each micro-robot body to enable subsequent deposition of a thin gold disc on the bottom inner wall of the micro-robot by electron beam vapor deposition. A mask fabricated over the micro-robot exposes the target region while shielding the rest of the structure during the deposition process. After two-photon exposure, the written structures are developed in a bath of isopropyl alcohol for 15 minutes. A second alcohol bath ensures that no photoresist remains inside the hollow body of each micro-robot.

The developed structures are subjected to electron beam physical vapor deposition to embed a thin metal layer inside the body of each micro-robot. First a 1 nm layer of titanium is deposited as adhesion layer followed by 5 nm layer of gold. The deposited metal layer is a circular disk of radius 8 μm. The fabrication process of the new micro-robots is summarized in Figure 5.5.

(a) two-photon-polymerization of microtools and masks
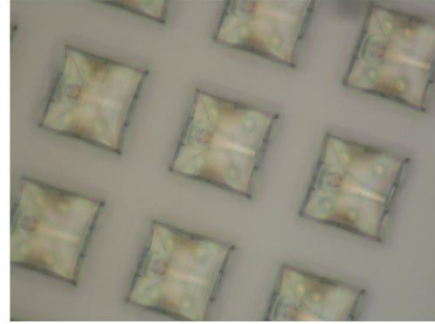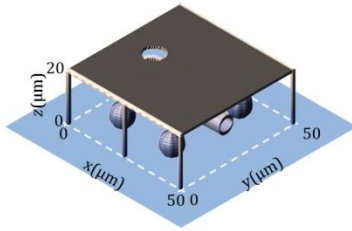
(b) electron beam physical vapor deposition
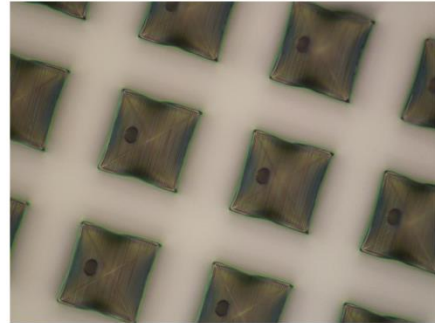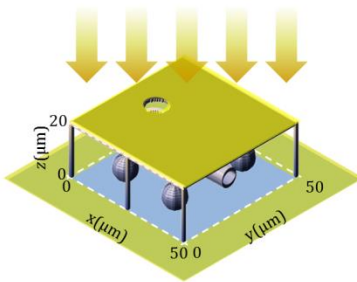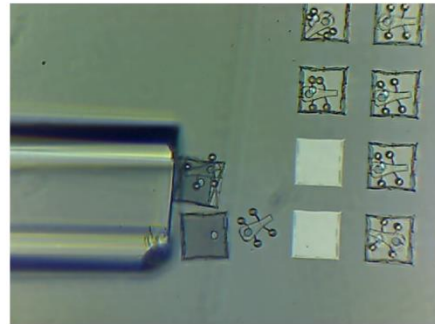
(c) collection of microtools
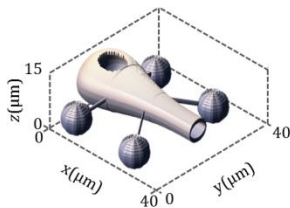
Figure 5.5. Fabrication process for the metal-embedded micro-robot. (a) The process starts with fabricating the micro-robots with two-photon polymerization process. A mask is also fabricated on top of each micro-robot to expose the region where the metal-layer is to be deposited. (b) The development of the micro-robots is

followed by electron beam physical vapor deposition of 1 nm layer of titanium followed by 5 nm of gold. (c) Selected micro-robots are collected from the substrate and transferred to a cytometry cuvette for trapping and loading/unloading experiments. Image is adapted from [130]

5.1.4. Sample preparation

The fabricated micro-robots are anchored to the glass substrate. A glass capillary tube attached to a microliter syringe is used to dislodge and collect a few of the micro-robots. The same syringe loads the micro-robots into a cytometry cuvette (Hellma, 250 μm × 250 μm inner cross section) containing a solution of deionized water, 0.5% Tween 80 surfactant and 10% ethanol. The process is performed under the microscope and, thus, transfer efficiency can be as high as 100% due to the selective and interactive picking approach. Unused micro-robots remain safely anchored to the substrate for succeeding experiments. Figure 5.6 shows a more detailed description of the collection process.
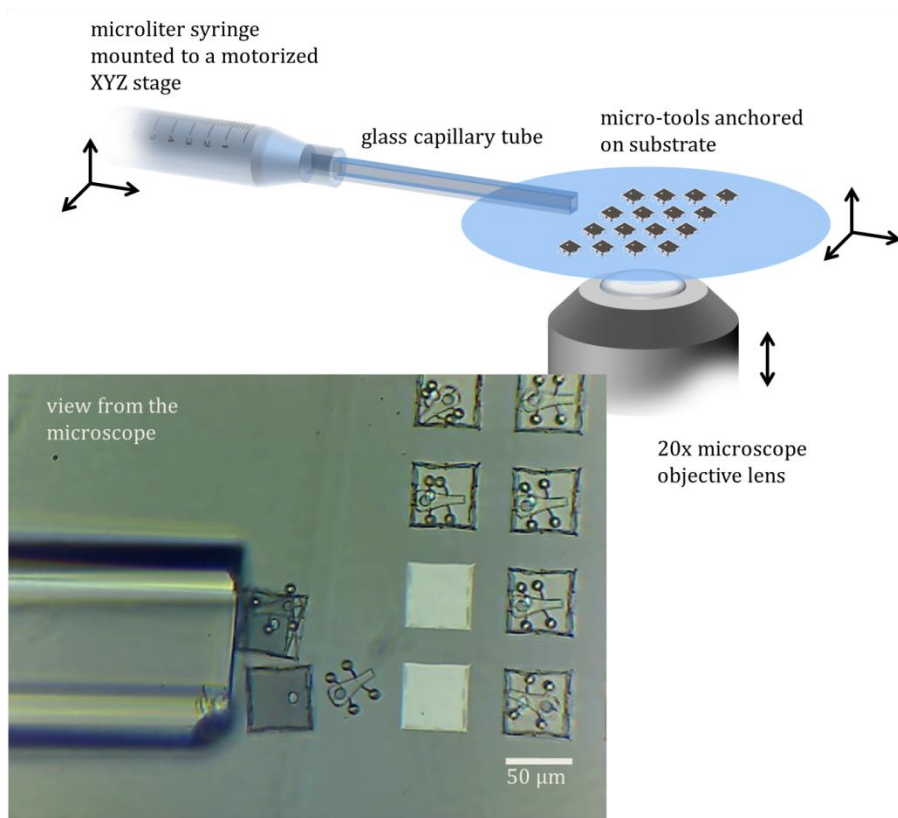
Figure 5.6. Collection of micro-robots. A fine glass capillary tube is fitted to a microliter syringe to dislodge and collect the micro-tools. The movement and pumping of the syringe are controlled by motorized actuators. The interactive collection mechanism employed in our setup allows up to 100% transfer efficiency. Image is adapted from [130].

5.2. Loading and unloading of cargo

Once samples are loaded in the cytometry cuvette, we perform optical manipulation and loading/unloading of cargo. In this section, we present the experimental results showing the loading and unloading of the micro-robot by optical means.

5.2.1. Optical manipulation and light-induced thermal convection

Optical trapping and manipulation experiments are performed on the BioPhotonics Workstation (see Figure 5.7). As with the previous chapters, the micro-robots are manipulated by counter-propagating traps. The BioPhotonics Workstation also generates an additional trapping beam, which is "repurposed" to illuminate the thin metal layer inside each structure, which then serves as a light-activated heating element for the fluid inside the micro-robot. The laser power at the sample plane needed to initiate convection is observed to occur starting at 17 mW. Videos of the experiments are grabbed from the top-view and selected snapshots are presented in this thesis.

Figure 5.7 Schematic showing the BioPhotonics Workstation for optical trapping, manipulation and actuation of a micro-tool. (a) The Biophotonics Workstation generat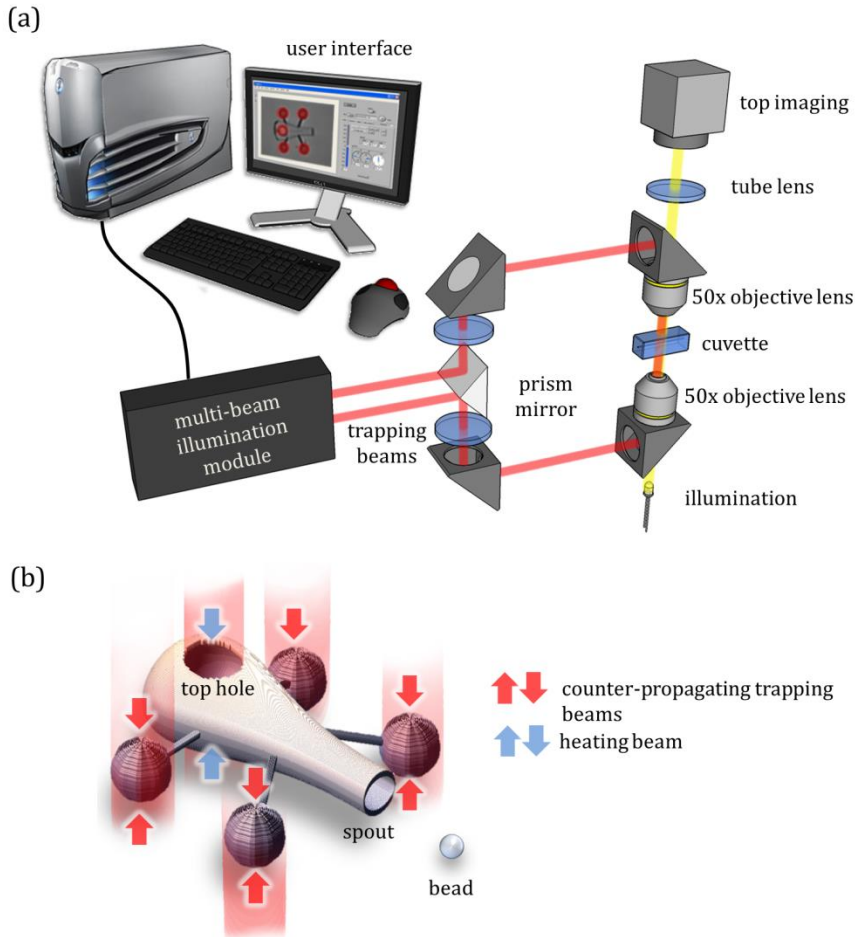es counter-propagating beam traps using a multi-beam illumination module. The top and bottom set of counter-propagating beams are imaged in the cuvette through opposing 50x objective lenses. The top imaging is fed real-time to the user-interface for intuitive optical manipulation. (b) Once loaded in the cuvette, optical manipulation of the micro-tools is done using real-time configured counter-propagating beams for each sphere handles. The use of multiple trapping beams allows tool movements with full six-degrees-of-freedom actuation and it is controlled by a LabVIEW-based user interface. An extra beam aimed at the micro-tool's top hole is used for heating the thin metallic layer. Image is adapted from [130].

Each of our micro-robots was designed to function as a vessel that can be moved with optical traps in real-time. Proof-of-principle experiments demonstrate that each of them can be used to load and unload cargo using laser-induced thermal convection. When the thin metal layer is heated with one of the available trapping beams, we observed that the heat generated is enough to produce strong convection currents that can pull 2μm-diameter silica and 1μm-diameter polystyrene beads towards the spout of the tools. We show in Figure 5.8 an illustrative flow speed measurement for a silica bead starting from outside the micro-robot until it enters its body. We observed flow speeds of around 10 μm s^{-1} near the opening which slows down as it moves towards the bigger cross section in accordance with the continuity equation. Near the heating element, the flow speed reaches more than 25 μm s^{-1}. This is greater than previously reported flow speeds generated by two-photon fabricated rotors acting as micropumps [22].

Thermal convection due to photothermal heating involves both photonic and fluidic phenomena. Multi-physics computer modeling of plasmonic heating elements having dimensions less than 200 nm predicts flow speeds of around 10 nm s^{-1} and it has been suggested that heating

elements should be greater than 1 μm for microfluidic applications [127] (we used 8 μm diameter). The convection current that draws particles into our micro-tools can be the combined result of natural and Marangoni convection [131]. The temperature gradient from the light-heated metal layer can directly create natural convection but it can also create a surface tension gradient along a microbubble surface. The surface tension gradient due to the temperature difference between the top and bottom surfaces of a bubble leads to Marangoni convection, which can be very strong [121]. Once the particle touches the microbubble, surface tension force essentially traps the particle and thus prevents it from coming out. A study of particle assembly on sandwiched colloidal suspension using Marangoni convection reports a maximum flow velocity at the gas/liquid interface to be as high as ~0.3 m s^{-1}. Away from the bubble there is a significant slowdown on the velocity [131]. The trend in our flow speed measurement of a tracer particle while it is being dragged by the convective flow (Figure 5.8) is consistent with this observation. An increase of 1-2 orders of magnitude on the mass transfer has also been observed for dissolved molecules [132].

Photothermal particles and thin metal films have been previously used in microfluidics for heat-induced flow control, sorting and mixing. However, the precise spatial control of particles' motion and locations such as placing them where and when they are needed can be challenging for smaller particles [133]. Moreover, thin metal films deposited on fixed regions within microfluidic channels completely lack the maneuverability that we show here. In short, our approach demonstrates a solution to this challenge by integrating the thin metal film within each light-controlled micro-tool that can readily function to transport cargo.

In our experiments, laser-induced heating of the metallic layer is able to form a microbubble inside the body of each micro-tool. Such microbubble formation is known to occur at temperatures between 220 and 240 °C for an array of nanoparticles and it is more or less invariant with the size of the illuminated area and incident laser power [134]. Moreover, we have observed that some of the polystyrene beads captured by a micro-tool can be melted by continuously heating the

fluid. No damage has been observed on neither micro-tools nor metal layers from the photothermal heating.
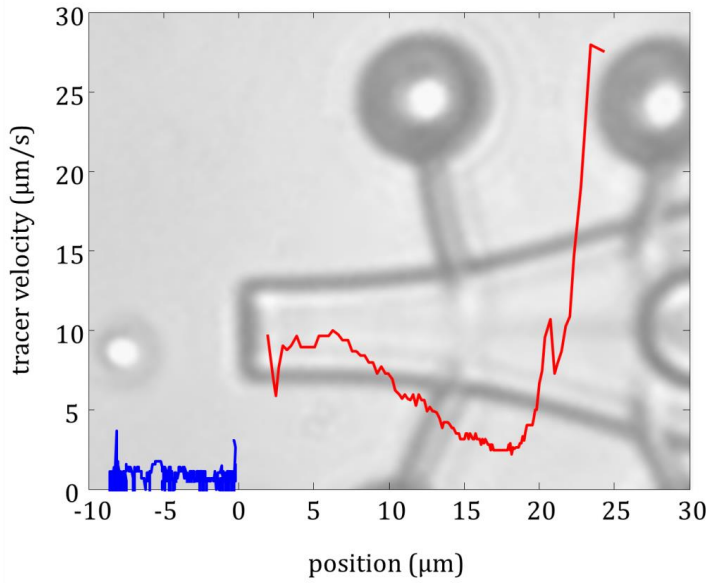
Figure 5.8. Flow speed measurement. The thin metal layer inside the body of each micro-tool is heated with a laser beam (1070 nm), which, in turn, creates a microbubble and generates strong thermal convection currents that gradually draw the cargo towards the spout of the micro-tool. We use a feature tracking algorithm to monitor the movement of the beads. The zero position is set at the spout of the micro-tool. The clear gap observed in the velocity plot is due to the limitation of the tracking algorithm to identify the bead when it crosses the dark outline of the micro-tool. The blue and red plots represent the velocity of a bead while it is outside and inside of the micro-tool, respectively. An image of a micro-tool is added to give a scale-indication of the horizontal axis. Image is adapted from [130].

Continuous illumination generates strong thermal convection currents that pull surrounding particles toward a laser-induced microbubble. Others have shown the feasibility of exploiting this for material

transport, e.g., direct-writing of patterned particle assemblies. It has been reported that dragging a microbubble with a heating CW laser beam can collect and deposit particles along its path to accomplish direct-writing of patterned particle assemblies [126]. Our tool utilizes the same principle with the advantage of greater selectivity and control over the particle collection since the design of the tool limits the direction of convective flow. In Figure 5.9, we demonstrate spatial control of the micro-tool by picking up scattered silica beads. The particle velocities we have measured for our micro-tool is significantly larger compared to using an optical trap alone. We have therefore exploited the conversion of optical energy to heat and, consequently, to kinetic energy via hydrodynamic effects to realize a new light-based micro-tool capable of performing controlled mechanical interactions with its surrounding micro-world in a way that goes beyond the limitations of conventional optical trapping. Whereas conventional optical trapping requires sufficient refractive index contrast between the captured particles and their surrounding medium, our method does not suffer from this inherent limitation. Potentially unwanted radiation effects to the sample can also be minimized or prevented.
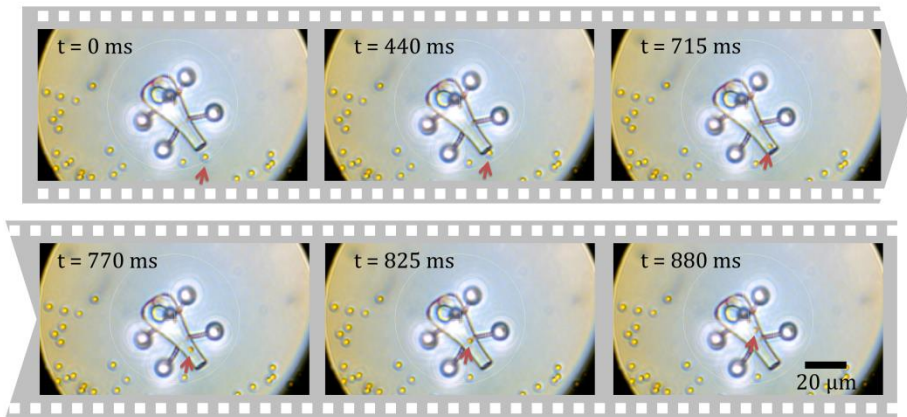

Figure 5.9. Loading of cargo using photothermal induced convection. Due to the spatial control provided by optical manipulation, the light robot can pick up cargo at different locations. Image is adapted from [130].

Upon loading cargo inside the tool and conveniently moving the tool to another location by optical micromanipulation, our experiments show that we can also exploit light-induced processes to eject captured particles. Figure 5.10 shows experiment results demonstrating that the cargo can be ejected by slightly moving the heating beam across the body of the micro-tool to perturb the microbubble to pump fluids with the particles out of the structure. This functionality mimics the familiar action of pumping a syringe. It has been observed that bubbles get attracted to regions of higher temperature in a phenomenon called thermocapillary bubble migration [121]. The attraction of the bubble to a heat source is very strong (i.e. up to an order of magnitude stronger than optical forces) thus it is feasible to use thermocapillary bubble migration as control for pumping. Trapping of bubbles has also been observed in more viscous molten glass medium where deformation of the bubble is the proposed trapping mechanism [135]. Some simulations have shown that the Marangoni convection can reverse when there are many particles adhering to the bubble [131]. This reversal of the Marangoni convection may also be present during unloading of cargo inside our micro-tools. Most studies are done on unconstrained Marangoni convection where there is a thin fluid film and the boundary is only at the bottom or both top and bottom surfaces. For our micro-tool, the fluid is practically constrained in all directions allowing only a small opening for the cargo and for the continuity of fluid flow to hold (i.e. top hole). Thus we expect nontrivial flow phenomenon that warrants further investigation. At this point, it suffices to say that the pumping action of the micro-tool is light-activated and to our knowledge this functionality has never been demonstrated before in a light-actuated micro-tool. Future work will explore new structure designs to optimize control over the convection processes constrained within them and even avoid ejecting particles out the top hole, which occasionally happens in the current design (e.g., covering the top hole with mesh-like features after metal deposition).
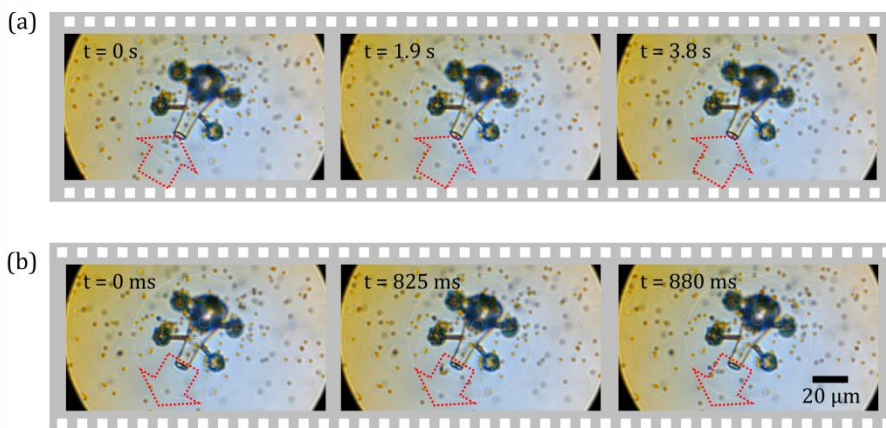
Figure 5.10. Micro-robot as pump. (a) A relatively large number of polystyrene beads (1 μm diameter) are dispersed in the trapping medium, and the micro-tool is used to collect them. (b) By changing the location of the heating beam, the micro-tool can be used to eject the captured particles by using the microbubble as a light-controlled piston. Image is adapted from [130].

5.3. Summary

In this chapter we have presented an integration of optical manipulation, two-photon fabrication and vapor deposition to create a new category for the toolbox of light robotics. We have embedded thin metal layers inside a plurality of light-driven micro-robots that enable the conversion of incident optical energy to heat and eventually hydrodynamic effects. Heating the metal layers generate thermal convection currents that can be used to load and unload cargo. We have demonstrated light-controlled pumping making each micro-robot suitable for material transport. A potential application that can fully utilize the capability of our new micro-robots is in drug delivery. Micro-machined devices with modified surface chemistry and morphology have already been successfully used in drug delivery [136]. Such devices are fabricated with a standard lithography process and have a planar geometry. However, using optically manipulated micro-sources can provide much better spatial and temporal selectivity as shown by experiments on cell stimulation via chemotaxis [137]. Such examples motivate the idea of a structure-mediated approach in biological studies

that use light-controlled, steered and actuated microstructures to mediate access to the sub-micron domain. Light robotics is an excellent candidate to realize these new functionalities in a fully flexible and dynamic context. The structural design freedom in two-photon fabrication can even adopt micro-needle structures that are commonly used for transdermal drug delivery [138] as an approach to advanced intracellular drug delivery.

Since the operation of our first batch of novel internally functionalized micro-robots demonstrated here is based on photothermal heating, resonant plasmonic structures can be readily integrated and used in future light robotic tools for more efficient heating and wavelength selectivity. The metal coating can be added on the spout of the micro-robot and can also be heated up once in contact with a cell of interest. It has been proposed in transfection experiments that heating of the cell membrane induces phase changes in the lipid layer and thus allow entry of foreign material. Our micro-robots do not preclude the possibility of being loaded prior to introduction to the trapping medium thus it is also possible to have micro-robots with different chemicals and perform precise chemical stimulation not possible in a standard cell culture.

6. Conclusion and outlook

Various methods and technologies can be integrated to build and control optically-actuated micro-robots or light robots that can perform specialized tasks. Microfluidics, plasmonics, optical manipulation and fabrication have already found successful applications in their respective areas. However, combining them not only presents new challenges, but also new and exciting ways to enable disruptive functionalities that would otherwise be difficult to realize by each sub-discipline in isolation.

We have presented two types of micro-robots: one for light delivery and another for material delivery. In both of these micro-robots we use various techniques such as beam shaping for optical manipulation and efficient illumination. Matter shaping is in the form of two-photon fabrication that is used in fabricating the micro-robots. We have successfully demonstrated targeted-light delivery in with our wave-guided optical waveguides (WOWs). This is accomplished with the use of holographic addressing and further improved with the Generalized Phase Contrast method. The micro-robot for material transport uses vapor deposition to embed a thin metal layer inside the body of the tool. The purpose is to improve photothermal heating to generate convection currents that can draw cargo in and out of the structure. The use of photothermal-induced convection current as loading mechanism overcomes the scaling of physical effects at small dimensions such as adhesion. Simply miniaturizing a syringe will not work in this case. We have successfully demonstrated that we can load and unload cargo using optical means.

As part of an on-going work, preliminary studies on the interaction of these micro-robots with live samples (e.g. yeast cells) has been made. To see different trapping scenarios, we have placed both of them in the same trapping medium. Our initial results suggest that they can coexist and the micro-robots can mechanically perturbed living organisms (see Figure 6.1)
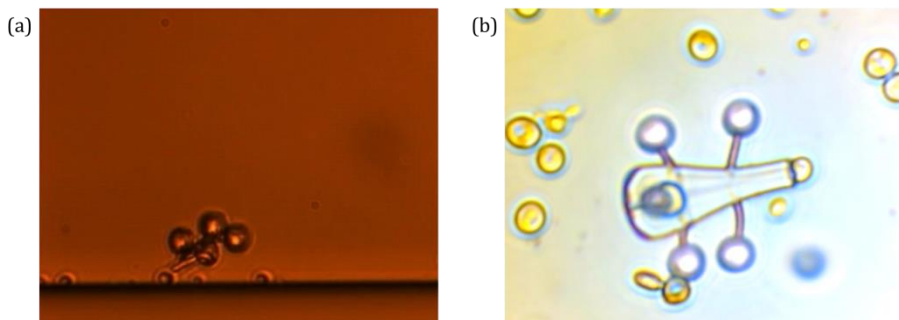
Figure 6.1. Light-driven micro-robots interacting with biological samples. (a) A wave-guided optical waveguide poking and delivering 532 nm light (filtered) to a yeast cell. (b) A hollow micro-tool using syringe action to hold a yeast cell in its spout.

Feynman envisioned many years ago independently controlled micro-machines performing noninvasive *in vivo* surgery. There has been interest in understanding diseases such as circulating tumor cells, which are very rare in blood samples. Because of their rarity, bulk measurement will average out the unique signature of this type of cell [64]. Our micro-tools can work in plurality and even with other micro-tools of different functionality to probe this single cell to investigate cellular responses to spatially or temporally correlated mechanical or chemical stimulation. The micro-robots presented here demonstrate the possibility of realizing this application. The light and matter shaping techniques used in this thesis are both very flexible, which makes rapid prototyping of different structures tailored for specific functionalities possible. We envision these micro-robots to be an important addition to the current tools in understanding biology in the micro-scale.

7. Appendix

7.1. Parametric equations for 3D printing

The micro-robots presented in this thesis are fabricated using a commercial two-photon polymerization (2PP) setup (Nanoscribe Photonic Professional, Nanoscribe GmbH, Germany). The photoresist (IP-L 780) is prepared over a microscope cover slip by drop casting. A pulsed laser (780 nm, 140 mW average power, 100 fs pulse duration) is used to induce two-photon absorption in the photoresist and creates a solid voxel. The laser or the stage can be scanned in 3D in order to "write" intended structures within the photoresist. In our particular setup, we use a piezo stage to do the scanning. The scanning trajectory can be set by the Cartesian coordinates that define our structures. In a raster scanning approach, these coordinates are extracted by slicing volumetric structure data from CAD software and then writing the structure line by line, layer by layer, from bottom to top, until the structure is fully printed. An alternative approach is to use directional scanning where the trajectory is the contour of the structure itself. We find that it is simpler to define our structure based on parametric equations that give the coordinates in a sequential manner based on some monotonically increasing parameters. As an example, consider the hollow body of our micro-robot for material transport. It is based on the surface of revolution of the so-called teardrop curve, which we parametrized as

$$
\begin{aligned}
x &= A\cos\theta \\
y &= \left[B\sin\theta\sin^m \tfrac{1}{2}\theta + r \right]\cos\phi \\
z &= \left[C\sin\theta\sin^m \tfrac{1}{2}\theta + r \right]\sin\phi
\end{aligned}
\tag{7.1}
$$

where $A = 20\,\mu m$, $B = 12\,\mu m$, and $C = 8\,\mu m$. The parameters $\theta = 0, \pi$ and $\phi = 0, 2\pi$ are sampled at 100 points within their respective range. The sampling interval is related to the hatching and slicing distance in the traditional raster scanning approach mentioned above. The radius of the spout is set to $r = 3\,\mu m$ and the taper towards the spout is determined by the parameter m which we set equal to 5. A hole with a diameter of 8 μm is left open on top of each micro-robot body for the subsequent deposition of thin gold disk on the bottom inner wall by

electron beam vapor deposition. A mask with matching hole (see Figure 7.1b) is fabricated on top of the micro-robot, held by support posts anchored to the substrate, to expose only the target region while shielding the rest of the micro-robot during the deposition process. For the WOWs, the bent part of the waveguide is from a quarter of a toroid followed by a series of straight lines for the rest of the waveguide and finally terminating with a cone. The spherical handles for optical trapping have diameters of 8 μm for both micro-robots.

In Figure 7.1a, we show a schematic of the micro-robot as it is being fabricated on top of the glass substrate. Thin supporting feet below each spherical handle ensure that the micro-robots are anchored firmly to the glass substrate. These feet are made by fabricating closely spaced vertical lines until they merge into a solid square bar with cross-sectional area of 1 μm × 1 μm and has height of 9 μm. This is important to keep the micro-robots from floating during development but can be dislodged easily during collection

The micro-robots are fabricated at 60% laser power and 50 μm s^{-1} while the mask for the material transport micro-robot is set to 70% laser power and 100 μm s^{-1} scan speed. The chosen laser power and scan is a good compromise between fabrication time and accuracy. The schematic diagram in Figure 7.1a shows only a few support posts for the mask for visual clarity but more are actually added for structural integrity and to minimize warping during development (see the SEM image in Figure 7.1d). The mask is fabricated 20 μm from the substrate to have sufficient gap from the micro-robot since we want the mask and the micro-robot to be separated during collection.

We are able to fabricate a 6 × 6 array of micro-robots for material transport and mask in about five hours. Figure 7.1c shows a brightfield image and Figure 7.1d shows a SEM image. The SEM image also shows more details in the structure of the mask. The WOWs are fabricated in a 7 × 12 array in four hours. After two-photon exposure, the written structures are developed in a bath of isopropyl alcohol for 15 minutes. A second alcohol bath is done for the hollow micro-robots to ensures that no photoresist remains inside.

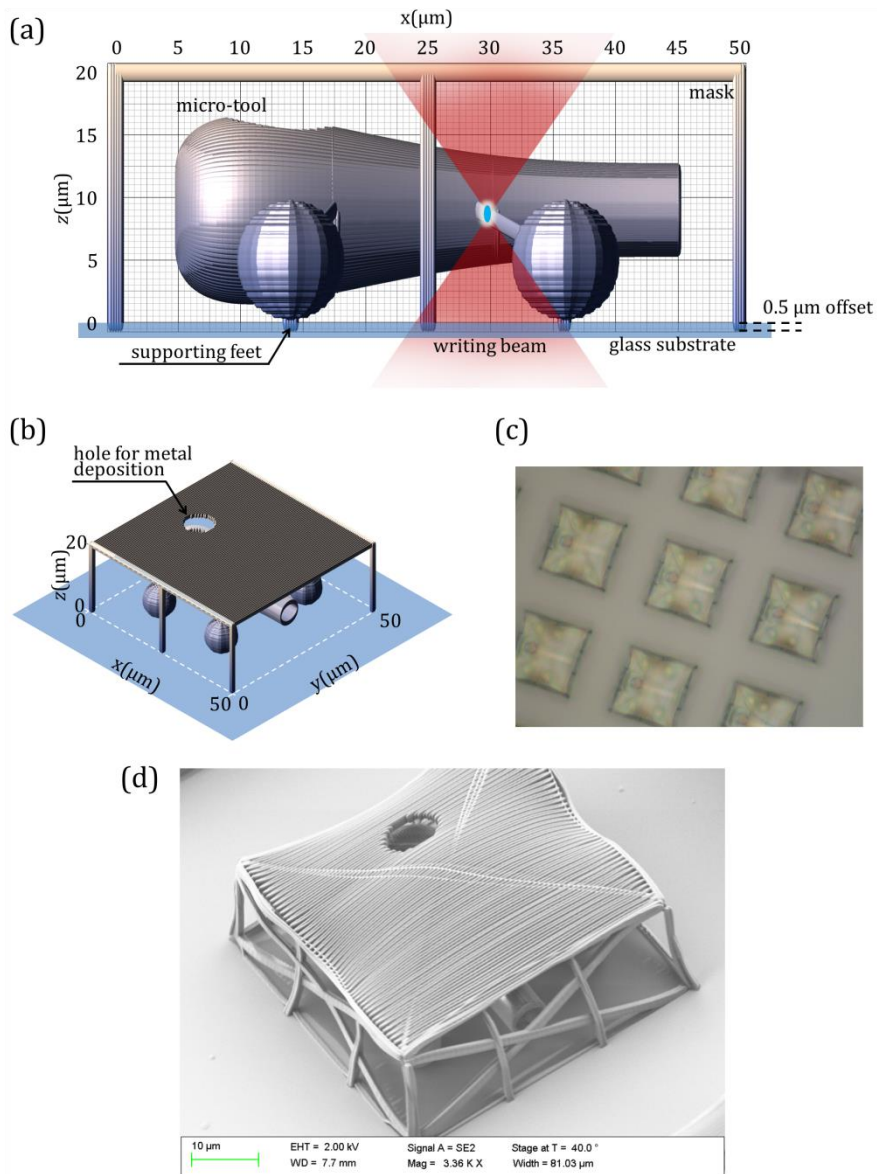**Figure 7.1.** (a) Schematic diagram of the 2PP fabrication of masks and micro-robots. They are fabricated on top of a microscope cover slip. An offset is made to ensure that the structure is anchored properly. (b) The hole on the mask is seen when viewing from a different angle. This hole exposes the target region where deposition will take place. (c) Brightfield and d) SEM images of the fabricated micro-robot.

Bibliography

1. R. P. Feynman, "There's plenty of room at the bottom," Resonance **16**, 890–905 (2011).
2. R. Feynman, "Infinitesimal Machinery," J. Microelectromechanical Syst. **2**, 4–14 (1993).
3. M. Wautelet, "Scaling laws in the macro-, micro- and nanoworlds," Eur. J. Phys. **22**, 601–611 (2001).
4. G. A. Ozin, I. Manners, S. Fournier-Bidoz, and A. Arsenault, "Dream nanomachines," Adv. Mater. **17**, 3011–3018 (2005).
5. J. J. Abbott, Z. Nagy, F. Beyeler, and B. J. Nelson, "Robotics in the Small, Part I: Microbotics," IEEE Robot. Autom. Mag. **14**, 92–103 (2007).
6. M. Sitti, "Microscale and Nanoscale Robotic Systems," IEEE Robot. Autom. Mag. **14**, 53 (2007).
7. W. F. Paxton, S. Sundararajan, T. E. Mallouk, and A. Sen, "Chemical locomotion," Angew. Chemie - Int. Ed. **45**, 5420–5429 (2006).
8. W. F. Paxton, K. C. Kistler, C. C. Olmeda, A. Sen, S. K. St. Angelo, Y. Cao, T. E. Mallouk, P. E. Lammert, and V. H. Crespi, "Catalytic nanomotors: Autonomous movement of striped nanorods," J. Am. Chem. Soc. **126**, 13424–13431 (2004).
9. A. A. Solovev, W. Xi, D. H. Gracias, S. M. Harazim, C. Deneke, S. Sanchez, and O. G. Schmidt, "Self-Propelled Nanotools," ACSNano **6**, 1751–1756 (2012).
10. W. Zhu, J. Li, Y. J. Leong, I. Rozen, X. Qu, R. Dong, Z. Wu, W. Gao, P. H. Chung, J. Wang, and S. Chen, "3D-Printed Artificial Microfish," Adv. Mater. **27**, 4411–4417 (2015).
11. Á. Barroso, S. Landwerth, M. Woerdemann, C. Alpmann, T. Buscher, M. Becker, A. Studer, and C. Denz, "Optical assembly of bio-hybrid micro-robots.," Biomed. Microdevices **17**, 9933 (2015).
12. Y. Mei, A. a Solovev, S. Sanchez, and O. G. Schmidt, "Rolled-up nanotech on polymers: from basic perception to self-propelled catalytic microengines.," Chem. Soc. Rev. **40**, 2109–2119 (2011).
13. D. Fan, Z. Yin, R. Cheong, F. Q. Zhu, R. C. Cammarata, C. L. Chien, and A. Levchenko, "Subcellular-resolution delivery of a cytokine through precisely manipulated nanowires.," Nat. Nanotechnol. **5**, 545–551 (2010).
14. S. Campuzano, D. Kagan, J. Orozco, and J. Wang, "Motion-driven sensing and biosensing using electrochemically propelled nanomotors," Analyst **136**, 4621 (2011).
15. K. Kim, J. Guo, X. Xu, and D. L. Fan, "Recent Progress on Man-Made Inorganic Nanomachines," Small **11**, 4037–4057 (2015).
16. A. Ashkin, J. M. Dziedzic, J. E. Bjorkholm, and S. Chu, "Observation

of a single-beam gradient force optical trap for dielectric particles.," Opt. Lett. **11**, 288 (1986).

17. D. Palima and J. Glückstad, "Gearing up for optical microrobotics: micromanipulation and actuation of synthetic microstructures by optical forces," Laser Photon. Rev. **7**, 478–494 (2013).

18. S. Kawata, H. B. Sun, T. Tanaka, and K. Takada, "Finer features for functional microdevices.," Nature **412**, 697–8 (2001).

19. S. Maruo, O. Nakamura, and S. Kawata, "Three-dimensional microfabrication with two-photon-absorbed photopolymerization.," Opt. Lett. **22**, 132–4 (1997).

20. P. Galajda and P. Ormos, "Complex micromachines produced and driven by light," Appl. Phys. Lett. **78**, 249 (2001).

21. L. Kelemen, S. Valkai, and P. Ormos, "Integrated optical motor.," Appl. Opt. **45**, 2777–2780 (2006).

22. S. Maruo and H. Inoue, "Optically driven micropump produced by three-dimensional two-photon microfabrication," Appl. Phys. Lett. **89**, 144101 (2006).

23. G. A. Swartzlander, T. J. Peterson, A. B. Artusio-Glimpse, and A. D. Raisanen, "Stable optical lift," Nat. Photonics **5**, 48–51 (2011).

24. J. Glückstad, "Optical manipulation: Sculpting the object," Nat. Photonics **5**, 7–8 (2011).

25. H. Zeng, P. Wasylczyk, C. Parmeggiani, D. Martella, M. Burresi, and D. S. Wiersma, "Light-Fueled Microscopic Walkers," Adv. Mater. (2015).

26. J. Liesener, M. Reicherter, T. Haist, and H. J. Tiziani, "Multi-functional optical tweezers using computer-generated holograms," Opt. Commun. **185**, 77–82 (2000).

27. E. R. Dufresne, G. C. Spalding, M. T. Dearing, S. A. Sheets, and D. G. Grier, "Computer-generated holographic optical tweezer arrays," Rev. Sci. Instrum. **72**, 1810–1816 (2001).

28. J. E. Curtis, B. A. Koss, and D. G. Grier, "Dynamic holographic optical tweezers," Opt. Commun. **207**, 169–175 (2002).

29. R. Eriksen, V. Daria, and J. Gluckstad, "Fully dynamic multiple-beam optical tweezers.," Opt. Express **10**, 597–602 (2002).

30. P. J. Rodrigo, V. R. Daria, and J. Glückstad, "Four-dimensional optical manipulation of colloidal particles," Appl. Phys. Lett. **86**, 1–3 (2005).

31. H.-U. Ulriksen, J. Thøgersen, S. Keiding, I. R. Perch-Nielsen, J. S. Dam, D. Z. Palima, H. Stapelfeldt, and J. Glückstad, "Independent trapping, manipulation and characterization by an all-optical biophotonics workstation," J. Eur. Opt. Soc. Rapid Publ. **3**, 08034 (2008).

32. M. Persson, D. Engström, and M. Goksör, "Real-time generation of

fully optimized holograms for optical trapping applications," in *Proc. of SPIE Vol. 8097*, K. Dholakia and G. C. Spalding, eds. (2011), Vol. 8097, p. 80971H.

33.   S. C. Chapin, V. Germain, and E. R. Dufresne, "Automated trapping, assembly, and sorting with holographic optical tweezers.," Opt. Express **14**, 13095–13100 (2006).

34.   P. J. Rodrigo, L. Kelemen, C. A. Alonzo, I. R. Perch-Nielsen, J. S. Dam, P. Ormos, and J. Glückstad, "2D optical manipulation and assembly of shape-complementary planar microstructures.," Opt. Express **15**, 9009–9014 (2007).

35.   P. J. Rodrigo, L. Kelemen, D. Palima, C. A. Alonzo, P. Ormos, and J. Glückstad, "Optical microassembly platform for constructing reconfigurable microenvironments for biomedical studies.," Opt. Express **17**, 6578–83 (2009).

36.   T. N. Buican, M. J. Smyth, H. a Crissman, G. C. Salzman, C. C. Stewart, and J. C. Martin, "Automated single-cell manipulation and sorting by light trapping.," Appl. Opt. **26**, 5311–5316 (1987).

37.   M. M. Wang, E. Tu, D. E. Raymond, J. M. Yang, H. Zhang, N. Hagen, B. Dees, E. M. Mercer, A. H. Forster, I. Kariv, P. J. Marchand, and W. F. Butler, "Microfluidic sorting of mammalian cells by optical force switching.," Nat. Biotechnol. **23**, 83–7 (2005).

38.   I. Perch-Nielsen, D. Palima, J. S. Dam, and J. Glückstad, "Parallel particle identification and separation for active optical sorting," J. Opt. A Pure Appl. Opt. **11**, 034013 (2009).

39.   P. J. Rodrigo, L. Gammelgaard, P. Bøggild, I. Perch-Nielsen, and J. Glückstad, "Actuation of microfabricated tools using multiple GPC-based counterpropagating-beam traps," Opt. Express **13**, 6899–6904 (2005).

40.   D. B. Phillips, J. A. Grieve, S. N. Olof, S. J. Kocher, R. Bowman, M. J. Padgett, M. J. Miles, and D. M. Carberry, "Surface imaging using holographic optical tweezers," Nanotechnology **22**, 285503 (2011).

41.   L. Ikin, D. M. Carberry, G. M. Gibson, M. J. Padgett, and M. J. Miles, "Assembly and force measurement with SPM-like probes in holographic optical tweezers," New J. Phys. **11**, 023012 (2009).

42.   D. B. Phillips, G. M. Gibson, R. Bowman, M. J. Padgett, S. Hanna, D. M. Carberry, M. J. Miles, and S. H. Simpson, "An optically actuated surface scanning probe," Opt. Express **20**, 29679–29693 (2012).

43.   D. B. Phillips, M. J. Padgett, S. Hanna, Y.-L. D. Ho, D. M. Carberry, M. J. Miles, and S. H. Simpson, "Shape-induced force fields in optical trapping," Nat. Photonics **8**, 400–405 (2014).

44.   G. Vizsnyiczai, T. Lestyán, J. Joniova, B. Aekbote, A. Strejčková, P. Ormos, P. Miskovsky, L. Kelemen, and G. Bano, "Optically Trapped

Surface-Enhanced Raman Probes Prepared by Silver Photo-Reduction to 3D Microstructures," Langmuir 150820173942008 (2015).

45. B. L. Aekbote, F. Schubert, P. Ormos, and L. Kelemen, "Gold nanoparticle-mediated fluorescence enhancement by two-photon polymerized 3D microstructures," Opt. Mater. (Amst). **38**, 301–309 (2014).

46. N. K. Metzger, M. Mazilu, L. Kelemen, P. Ormos, and K. Dholakia, "Observation and simulation of an optically driven micromotor," J. Opt. **13**, 044018 (2011).

47. D. Palima, A. R. Bañas, G. Vizsnyiczai, L. Kelemen, T. Aabo, P. Ormos, and J. Glückstad, "Optical forces through guided light deflections," Opt. Express **21**, 581–593 (2013).

48. S. L. Neale, M. P. MacDonald, K. Dholakia, and T. F. Krauss, "All-optical control of microfluidic components using form birefringence," Nat. Mater. **4**, 530–533 (2005).

49. S. H. Simpson, D. B. Phillips, D. M. Carberry, and S. Hanna, "Bespoke optical springs and passive force clamps from shaped dielectric particles," J. Quant. Spectrosc. Radiat. Transf. **126**, 91–98 (2013).

50. D. Preece, R. Bowman, A. Linnenberger, G. Gibson, S. Serati, and M. Padgett, "Increasing trap stiffness with position clamping in holographic optical tweezers.," Opt. Express **17**, 22718–25 (2009).

51. A. Bañas, O. Kopylov, M. Villangca, D. Palima, and J. Glückstad, "GPC light shaper: static and dynamic experimental demonstrations," Opt. Express **22**, 23759–69 (2014).

52. M. Villangca, A. Bañas, D. Palima, and J. Glückstad, "GPC-enhanced read-out of holograms," Opt. Commun. **351**, 121–127 (2015).

53. M. A. Taylor, M. Waleed, A. B. Stilgoe, H. Rubinsztein-dunlop, and W. P. Bowen, "Enhanced optical trapping via structured scattering," Nat. Photon. **9**, 669–674 (2015).

54. J. W. Goodman, *Introduction to Fourier Optics* (Roberts and Company Publishers, 2005).

55. D. Gabor, "A new microscopic principle.," Nature **161**, 777–778 (1948).

56. E. N. Leith and J. Upatnieks, "Reconstructed Wavefronts and Communication Theory," J. Opt. Soc. Am. **52**, 1123 (1962).

57. J. Curtis, B. A. Koss, and D. G. Grier, "Dynamic holographic optical tweezers," Opt. Commun. **207**, 169–175 (2002).

58. D. G. Grier, "A revolution in optical manipulation.," Nature **424**, 810–816 (2003).

59. K. Dholakia and T. Čižmár, "Shaping the future of manipulation,"

Nat. Photonics **5**, 335–342 (2011).

60. M. Woerdemann, C. Alpmann, M. Esseling, and C. Denz, "Advanced optical trapping by complex beam shaping," Laser Photon. Rev. **7**, 839–854 (2013).

61. M. A. Taylor, M. Waleed, A. B. Stilgoe, H. Rubinsztein-dunlop, and W. P. Bowen, "Enhanced optical trapping via structured scattering," Nat. Photon. **9**, 669–674 (2015).

62. A. Ashkin, "Acceleration and Trapping of Particles by Radiation Pressure," Phys. Rev. Lett. **24**, 156–159 (1970).

63. Y. Tsuda, O. Mori, R. Funase, H. Sawada, T. Yamamoto, T. Saiki, T. Endo, K. Yonekura, H. Hoshino, and J. Kawaguchi, "Achievement of IKAROS — Japanese deep space solar sail demonstration mission," Acta Astronaut. **82**, 183–188 (2012).

64. M. Villangca, D. Casey, and J. Glückstad, "Optically-controlled platforms for transfection and single- and sub-cellular surgery," Biophys. Rev. **7**, 379–390 (2015).

65. K. C. Neuman and S. M. Block, "Optical trapping.," Rev. Sci. Instrum. **75**, 2787–809 (2004).

66. H. Zhang and K.-K. Liu, "Optical tweezers for single cells.," J. R. Soc. Interface **5**, 671–90 (2008).

67. A. Rohrbach and E. H. K. Stelzer, "Trapping Forces, Force Constants, and Potential Depths for Dielectric Spheres in the Presence of Spherical Aberrations," Appl. Opt. **41**, 2494 (2002).

68. T. a Nieminen, V. L. Y. Loke, A. B. Stilgoe, G. Knöner, A. M. Brańczyk, N. R. Heckenberg, and H. Rubinsztein-Dunlop, "Optical tweezers computational toolbox," J. Opt. A Pure Appl. Opt. **9**, S196–S203 (2007).

69. C. C. Mao, K. M. Johnson, R. Turner, D. Jared, and D. Doroski, "Applications of Binary and Analog Hydrogenated Amorphous-Silicon Ferroelectric Liquid-Crystal Optically Addressed Spatial Light Modulators," Appl. Opt. **31**, 3908–3916 (1992).

70. P. M. P. Lanigan, I. Munro, E. J. Grace, D. Casey, J. Phillips, D. R. Klug, O. Ces, and M. A. A. Neil, "Dynamical hologram generation for high speed optical trapping of smart droplet microtools," Biomed. Opt. Express **3**, 1609–1619 (2012).

71. W. Hossack, E. Theofanidou, J. Crain, K. Heggarty, and M. Birch, "High-speed holographic optical tweezers using a ferroelectric liquid crystal microdisplay," Opt. Express **11**, 2053 (2003).

72. D. McGloin and K. Dholakia, "Bessel beams: Diffraction in a new light," Contemp. Phys. **46**, 15–28 (2005).

73. D. B. Ruffner and D. G. Grier, "Optical conveyors: A class of active tractor beams," Phys. Rev. Lett. **109**, 1–5 (2012).

74. H. Xin, R. Xu, and B. Li, "Optical trapping, driving, and

arrangement of particles using a tapered fibre probe.," Sci. Rep. **2**, 818 (2012).

75.   a Constable, J. Kim, J. Mervis, F. Zarinetchi, and M. Prentiss, "Demonstration of a fiber-optical light-force trap.," Opt. Lett. **18**, 1867–1869 (1993).

76.   P. J. Rodrigo, I. R. Perch-Nielsen, and J. Glückstad, "Three-dimensional forces in GPC-based counterpropagating-beam traps.," Opt. Express **14**, 5812–22 (2006).

77.   H.-U. Ulriksen, J. Thogersen, S. Keiding, I. R. Perch-Nielsen, J. S. Dam, D. Z. Palima, H. Stapelfeldt, and J. Glückstad, "Independent trapping, manipulation and characterization by an all-optical biophotonics workstation," J. Eur. Opt. Soc. Rapid Publ. **3**, 08034 (2008).

78.   G. Thalhammer, R. Steiger, S. Bernet, and M. Ritsch-Marte, "Optical macro-tweezers: trapping of highly motile micro-organisms," J. Opt. **13**, 044024 (2011).

79.   G. Lenormand and A. Richert, "A New Determination of the Shear Modulus of the Human Erythrocyte Membrane Using Optical Tweezers," Biophys. J. **76**, 1145–1151 (1999).

80.   H. Kress, J.-G. Park, C. O. Mejean, J. D. Forster, J. Park, S. S. Walse, Y. Zhang, D. Wu, O. D. Weiner, T. M. Fahmy, and E. R. Dufresne, "Cell stimulation with optically manipulated microsources.," Nat. Methods **6**, 905–9 (2009).

81.   M. J. Lang and S. M. Block, "Resource Letter: LBOT-1: Laser-based optical tweezers.," Am. J. Phys. **71**, 201–215 (2003).

82.   H.-B. Sun and S. Kawata, "Two-Photon Photopolymerization and 3D Lithographic Microfabrication," in *Advances in Polymer Science* (2006), Vol. 170, pp. 169–273.

83.   S. Kawata, "Two-photon laser precision microfabrication and its applications to micro-nano devices and systems," J. Light. Technol. **21**, 624–633 (2003).

84.   D. Palima, A. Bañas, G. Vizsnyiczai, L. Kelemen, P. Ormos, and J. Glückstad, "Wave-guided optical waveguides," Opt. Express **20**, 2004–2014 (2012).

85.   M. Villangca, A. Bañas, D. Palima, and J. Glückstad, "Dynamic diffraction-limited light-coupling of 3D-maneuvered wave-guided optical waveguides," Opt. Express **22**, 17880–17889 (2014).

86.   M. Villangca, A. Bañas, D. Palima, and J. Glückstad, "Generalized phase contrast-enhanced diffractive coupling to light-driven microtools," Opt. Eng. **54**, 111308 (2015).

87.   G. P. Agrawal, *Nonlinear Fiber Optics* (Academic Press, 2007).

88.   A. Melloni, P. Monguzzi, R. Costa, and M. Martinelli, "Design of curved waveguides: the matched bend," J. Opt. Soc. Am. A. Opt.

Image Sci. Vis. **20**, 130–137 (2003).

89. J. Kerttula, V. Filippov, V. Ustimchik, Y. Chamorovskiy, and O. G. Okhotnikov, "Mode evolution in long tapered fibers with high tapering ratio," Opt. Express **20**, 25461–70 (2012).

90. D. Palima and J. Glückstad, "Comparison of generalized phase contrast and computer generated holography for laser image projection.," Opt. Express **16**, 5338–5349 (2008).

91. M. Montes-Usategui, E. Pleguezuelos, J. Andilla, and E. Martín-Badosa, "Fast generation of holographic optical tweezers by random mask encoding of Fourier components," Opt. Express **14**, 2101–2107 (2006).

92. G. Siviloglou, J. Broky, a. Dogariu, and D. Christodoulides, "Observation of Accelerating Airy Beams," Phys. Rev. Lett. **99**, 213901 (2007).

93. D. McGloin and K. Dholakia, "Bessel beams: Diffraction in a new light," Contemp. Phys. **46**, 15–28 (2005).

94. J. Liesener, M. Reicherter, T. Haist, and H. J. Tiziani, "Multi-functional optical tweezers using computer-generated holograms," Opt. Commun. **185**, 77–82 (2000).

95. M. A. Go, C. Stricker, S. Redman, H.-A. Bachor, and V. R. Daria, "Simultaneous multi-site two-photon photostimulation in three dimensions.," J. Biophotonics **5**, 745–53 (2012).

96. J. Kato, N. Takeyasu, Y. Adachi, H.-B. Sun, and S. Kawata, "Multiple-spot parallel processing for laser micronanofabrication," Appl. Phys. Lett. **86**, 044102 (2005).

97. F. Bergermann, L. Alber, S. J. Sahl, J. Engelhardt, and S. W. Hell, "2000-fold parallelized dual-color STED fluorescence nanoscopy," Opt. Express **23**, 211 (2015).

98. A. Bañas, D. Palima, M. Villangca, T. Aabo, and J. Glückstad, "GPC light shaper for speckle-free one-and two-photon contiguous pattern excitation," Opt. Express **22**, 5299–5310 (2014).

99. A. Laskin, D. L. Shealy, and N. C. Evans, "Optimization- Based Designs," in *Laser Beam Shaping: Theory and Techniques*, F. Dickey, ed., 2nd ed. (CRC Press, 2014).

100. "piShaper - Versatile Beam Shaping Optics," http://www.pishaper.com/actual_news.php.

101. O. Kopylov, A. Bañas, M. Villangca, and D. Palima, "GPC light shaping a supercontinuum source," Opt. Express **23**, 1894–1905 (2015).

102. R. W. Gerchberg and W. O. Saxton, "A practical algorithm for the determination of phase from image and diffraction plane pictures," Optik (Stuttg). **35**, 237–246 (1972).

103. J. R. Fienup, "Phase retrieval algorithms: a comparison.," Appl.

Opt. **21**, 2758–69 (1982).

104.   J. Fienup and C. C. Wackerman, "Phase retrieval stagnation problems and solutions," J. Opt. Soc. Am. A **3**, 1897–1907 (1986).

105.   H. H. Bauschke, P. L. Combettes, and D. R. Luke, "Phase retrieval, error reduction algorithm, and Fienup variants: a view from convex optimization," J. Opt. Soc. Am. A **19**, 1334–45 (2002).

106.   G. Yang, B. Dong, B. Gu, J. Zhuang, and O. K. Ersoy, "Gerchberg-Saxton and Yang-Gu algorithms," **33**, 209–218 (1994).

107.   G. Sinclair, J. Leach, P. Jordan, G. Gibson, E. Yao, Z. Laczik, M. Padgett, and J. Courtial, "Interactive application in holographic optical tweezers of a multi-plane Gerchberg-Saxton algorithm for three-dimensional light shaping.," Opt. Express **12**, 1665–70 (2004).

108.   F. Belloni and S. Monneret, "Quadrant kinoform: an approach to multiplane dynamic three-dimensional holographic trapping.," Appl. Opt. **46**, 4587–93 (2007).

109.   P. L. Hilario, M. J. Villangca, and G. Tapang, "Independent light fields generated using a phase-only spatial light modulator.," Opt. Lett. **39**, 2036–9 (2014).

110.   G. Shabtay, "Three-dimensional beam forming and Ewald's surfaces," Opt. Commun. **226**, 33–37 (2003).

111.   G. Whyte and J. Courtial, "Experimental demonstration of holographic three-dimensional light shaping using a Gerchberg–Saxton algorithm," New J. Phys. **7**, 117–117 (2005).

112.   M. Persson, D. Engström, A. Frank, J. Backsten, J. Bengtsson, and M. Goksör, "Minimizing intensity fluctuations in dynamic holographic optical tweezers by restricted phase change.," Opt. Express **18**, 11250–11263 (2010).

113.   D. Oron, E. Papagiakoumou, F. Anselmi, and V. Emiliani, "Two-photon optogenetics.," in *Progress in Brain Research*, T. Knöpfel and E. Boyden, eds., 1st ed. (Elsevier B.V., 2012), Vol. 196, pp. 119–43.

114.   G. Bautista, M. J. Romero, G. Tapang, and V. R. Daria, "Parallel two-photon photopolymerization of microgear patterns," Opt. Commun. **282**, 3746–3750 (2009).

115.   S. Jeon, V. Malyarchuk, J. A. Rogers, and G. P. Wiederrecht, "Fabricating three-dimensional nanostructures using two photon lithography in a single exposure step.," Opt. Express **14**, 2300–8 (2006).

116.   K. Fukunaga and L. Hostetler, "The estimation of the gradient of a density function, with applications in pattern recognition," IEEE Trans. Inf. Theory **21**, 32–40 (1975).

117.   D. Comaniciu and P. Meer, "Mean shift: A robust approach toward

feature space analysis," IEEE Trans. Pattern Anal. Mach. Intell. **24**, 603–619 (2002).

118.   C. Poynton, *Digital Video and HDTV Algorithms and Interfaces* (Morgan Kaufmann Publishers Inc., 2003).

119.   R. N. Ghosh and W. W. Webb, "Automated detection and tracking of individual and clustered cell surface low density lipoprotein receptor molecules.," Biophys. J. **66**, 1301–1318 (1994).

120.   M. Villangca, D. Palima, A. Bañas, and J. Glückstad, "Photothermal heating in metal-embedded microtools for material transport," in *Proc. SPIE 9764, Complex Light and Optical Forces X*, J. Glückstad, D. L. Andrews, and E. J. Galvez, eds. (2016), Vol. 9764, p. 97641F.

121.   D. W. Berry, N. R. Heckenberg, and H. Rubinszteindunlop, "Effects associated with bubble formation in optical trapping," J. Mod. Opt. **47**, 1575–1585 (2000).

122.   K. Zhang, A. Jian, X. Zhang, Y. Wang, Z. Li, and H. Tam, "Laser-induced thermal bubbles for microfluidic applications," Lab Chip **11**, 1389 (2011).

123.   X. Miao, B. K. Wilson, and L. Y. Lin, "Localized surface plasmon assisted microfluidic mixing," Appl. Phys. Lett. **92**, 3–5 (2008).

124.   G. Baffou and R. Quidant, "Thermo-plasmonics: Using metallic nanostructures as nano-sources of heat," Laser Photonics Rev. **7**, 171–187 (2013).

125.   G. L. Liu, J. Kim, Y. Lu, and L. P. Lee, "Optofluidic control using photothermal nanoparticles.," Nat. Mater. **5**, 27–32 (2006).

126.   Y. Zheng, H. Liu, Y. Wang, C. Zhu, S. Wang, J. Cao, and S. Zhu, "Accumulating microparticles and direct-writing micropatterns using a continuous-wave laser-induced vapor bubble," Lab Chip **11**, 3816 (2011).

127.   J. Donner, G. Baffou, D. McCloskey, and R. Quidant, "Plasmon-Assisted Optofluidics," ACS Nano **5**, 5457–5462 (2011).

128.   E. W. Weisstein, "Surface of Revolution," (n.d.).

129.   E. W. Weisstein, "Teardrop Curve," (n.d.).

130.   M. J. Villangca, D. Palima, A. R. Bañas, and J. Glückstad, "Light-driven micro-tool equipped with a syringe function," Light Sci. Appl. (2016).

131.   L. Lin, X. Peng, Z. Mao, W. Li, M. N. Yogeesh, B. B. Rajeeva, E. P. Perillo, A. K. Dunn, D. Akinwande, and Y. Zheng, "Bubble-Pen Lithography," Nano Lett. acs.nanolett.5b04524 (2015).

132.   O. a Louchev, S. Juodkazis, N. Murazawa, S. Wada, and H. Misawa, "Coupled laser molecular trapping, cluster assembly, and deposition fed by laser-induced Marangoni convection.," Opt. Express **16**, 5673 (2008).

133.   A. a. Kayani, K. Khoshmanesh, S. a. Ward, A. Mitchell, and K.

Kalantar-zadeh, "Optofluidics incorporating actively controlled micro- and nano-particles," Biomicrofluidics **6**, 031501 (2012).

134. G. Baffou, J. Polleux, H. Rigneault, and S. Monneret, "Super-heating and micro-bubble generation around plasmonic nanoparticles under cw illumination," J. Phys. Chem. C **118**, 4890–4898 (2014).

135. N. Murazawa, S. Juodkazis, H. Misawa, and H. Wakatsuki, "Laser trapping of deformable objects.," Opt. Express **15**, 13310–7 (2007).

136. S. L. Tao and T. a. Desai, "Micromachined devices: The impact of controlled geometry from cell-targeting to bioavailability," J. Control. Release **109**, 127–138 (2005).

137. H. Kress, J. J.-G. Park, C. O. Mejean, J. D. Forster, J. J.-G. Park, S. S. Walse, Y. Zhang, D. Wu, O. D. Weiner, T. M. Fahmy, and E. R. Dufresne, "Cell stimulation with optically manipulated microsources.," Nat. Methods **6**, 905–9 (2009).

138. S. D. Gittard, A. Ovsianikov, B. N. Chichkov, A. Doraiswamy, and R. J. Narayan, "Two-photon polymerization of microneedles for transdermal drug delivery," Expert Opin. Drug Deliv. **7**, 513–533 (2010).